UNIVERSITAT POLITÈCNICA DE VALÈNCIA

Escuela Técnica Superior
de Ingeniería del Diseño

NUMERICAL DESIGN AND OPTIMIZATION
OF A RESCUE UAV'S WING

Bachelor's thesis

Aerospace Engineering

AUTHOR: Luis G. Sevillá Pastor

Tutor: Luca Marino

External cotutor: Xandra Margot

ACADEMIC YEAR: 2021-2022

Acknowledgements

First of all, I would like to thank prof. Luca Marino for guiding me these last few months in developing my thesis during my stay at Sapienza Università di Roma, for all of the knowledge and patience he has shared with me, and both courses I have had him in my last bachelor year.

Furthermore, I would also like to recognize the rest of the professors I have had at the ETSID in the UPV who have taught me these last 4 years, which have passed much faster than I realized, throughout my journey in the Aerospace Engineering bachelor, specially to prof. Xandra Margot, for her deeply interesting course in aerodynamics and her beautiful recommendation letter for my MSc application.

I am deeply grateful for all of the friends I have made during my university experience, without whom I would certainly not be here today, about to obtain my engineer title. I'd also like to make mention all of my Erasmus friends who have made this last year one of the bests in my life, specially to both my friends and roommates who I certainly consider family now.

Last but certainly not least, I could not have undertaken this odyssey without the constant love and encouragement of my family, specially those of my mother and brother. They have given me all of their unconditional support and have certainly help me achieve all of my goals these last, tough years.

Abstract

This final degree thesis focuses on the aircraft preliminary design aspect, specifically on the optimization of a maritime rescue UAV's wing. The work begins with an introduction explaining the migrant crisis in the Mediterranean Sea: migration routes, scale of the issue in numbers, and the current measures. Then the proposed solution is explained: to employ a rescue UAV capable of deploying life rafts. The conceptual design of the aircraft is built upon Marangoni's thesis in order to define the mission characteristics and overall performance of the UAV. Then, a market search is performed to find similar models, and more importantly, the airfoils used. After an analysis of these, the NACA 4415 is selected as the base airfoil. From there, the optimization process begins. The taper ratio, aspect ratio and swept angle is calculated to proceed with the twist. Prandtl's Lifting-Line theory, developed in Matlab, is used to obtain the optimal distribution of the twist along the wingspan. Finally, the geometric twist is implemented, creating the entire optimized wing, to then compare it with the base wing using the XFLR5 software to conclude with the overall improvement.

Index

List of Figures

List of Tables

Nomenclature

E	Aerodynamic efficiency
V	Aircraft flight speed
C_d	Airfoil drag coefficient
C_l	Airfoil lift coefficient
$C_{l,\alpha}$	Airfoil section lift slope
α	Angle of Attack
AoA	
AR	Aspect Ratio
L	Characteristic length
Γ	Circulation throughout wingspan
a_n	Component of the Fourier coefficient corresponding to the wing's planform
b_n	Component of the Fourier coefficient corresponding to the wing's twist
ρ	Density
C_{Ld}	Design wing lift coefficient
t/c	Dimensionless airfoil thickness
C_D	Drag coefficient
μ	Dynamic viscosity
α_{eff}	Effective angle of attack
h	Flight altitude
A_n	Fourier coefficients of the series expansion of the solution of the lifting line equation
V_∞	Free stream velocity
R	Gas constant
$\alpha(z)$	Geometric angle of attack
g	Gravity
α_i	Induced angle of attack
D_i	Induced drag
C_{D_i}	Induced drag coefficient
k_L	Lift slope factor
k_{DL}	Lift-washout contribution to the induced-drag factor
MTOW	Maximum Takeoff Weight
W_{TO}	
Ω	Maximum total washout
ω	Normalized washout distribution
k_{Do}	Optimum induced drag factor
Ω_{opt}	Optimum total washout to minimize induced drag factor
e	Oswald's efficiency factor
k_D	Planform contribution to the induced-drag factor
P	Power
η	Propulsive Efficiency
R	Range
Re	Reynolds number
c_{root}	Root chord
SM	*Salvamento Marítimo*
SAR	Search and Rescue
z	Spanwise coordinate
SFC	Specific fuel consumption
S_μ	Sutherland's constant
Λ	Sweep Angle
TR	Taper Ratio
T	Temperature

c_{tip}	Tip chord
ε_{Ω}	Twist effectiveness
UAV	Unmanned Aerial Vehicle
$k_{D\Omega}$	Washout contribution to the induced-drag factor
C_L	Wing lift coefficient
$C_{L,\alpha}$	Wing section lift slope
S	Wing surface area
b	Wingspan
α_{L0}	Zero lift angle of attack

1. Introduction

a. Mediterranean migration crisis

According to the International Organization for Migration (IOM), almost 200 thousand people ventured into the Mediterranean waters in an attempt to reach Europe from Africa last year alone [1]. In an ongoing global migration crisis, asylum seekers and migrants endanger their lives in a treacherous journey on unstable, unprotected boats guided by smugglers in what is considered one of the most dangerous and deadly migration routes in the world.

The Mediterranean is usually divided into three main routes: the central Mediterranean has been one of the primary migrant routes, and mainly refers to the fluxes of people leaving Libya and Tunisia hoping to reach Italy and Malta; the western Mediterranean route, which has seen a noticeable flow increase in recent years, consists of Morocco and Western Sahara migrants crossing to mainland Spain and the Canary Islands; lastly, the Eastern Mediterranean leads from Turkey to Greece, most predominantly Syrian refugees escaping their country's civil war [2]. the routes can be visualized in the map below (Figure 1.1) [3].
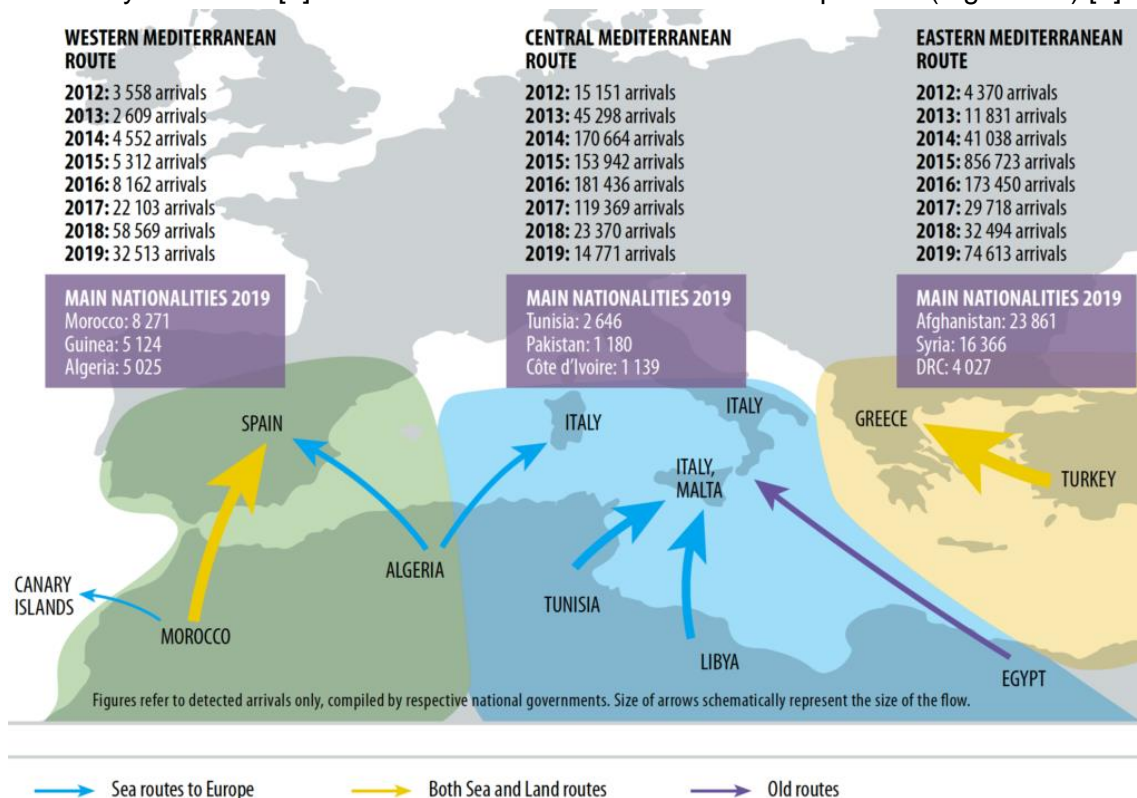
WESTERN MEDITERRANEAN ROUTE
2012: 3 558 arrivals
2013: 2 609 arrivals
2014: 4 552 arrivals
2015: 5 312 arrivals
2016: 8 162 arrivals
2017: 22 103 arrivals
2018: 58 569 arrivals
2019: 32 513 arrivals

MAIN NATIONALITIES 2019
Morocco: 8 271
Guinea: 5 124
Algeria: 5 025

CENTRAL MEDITERRANEAN ROUTE
2012: 15 151 arrivals
2013: 45 298 arrivals
2014: 170 664 arrivals
2015: 153 942 arrivals
2016: 181 436 arrivals
2017: 119 369 arrivals
2018: 23 370 arrivals
2019: 14 771 arrivals

MAIN NATIONALITIES 2019
Tunisia: 2 646
Pakistan: 1 180
Côte d'Ivoire: 1 139

EASTERN MEDITERRANEAN ROUTE
2012: 4 370 arrivals
2013: 11 831 arrivals
2014: 41 038 arrivals
2015: 856 723 arrivals
2016: 173 450 arrivals
2017: 29 718 arrivals
2018: 32 494 arrivals
2019: 74 613 arrivals

MAIN NATIONALITIES 2019
Afghanistan: 23 861
Syria: 16 366
DRC: 4 027

Figures refer to detected arrivals only, compiled by respective national governments. Size of arrows schematically represent the size of the flow.

→ Sea routes to Europe   → Both Sea and Land routes   → Old routes

Figure 1. 1: The three Mediterranean migration routes

According to the Missing Migrants Projects, an organization initiated by the IOM that documents the deaths and disappearances of people in the process of migration, there have been 24.184 missing migrants recorded in the Mediterranean since 2014. Out of this alarming number, a further distressing figure emerges: 16.584 of these are confirmed drowning cases [1]. It is because of this that the High Commissioner for the Human Rights of the United Nations has deemed the current situation as "non-viable and unsustainable" and having "devastating human consequences" [4].

b. Current Measures

Evaristo Álvarez, helicopter commander of the State Society for Salvage and Maritime Safety of Galicia (*Sociedad Estatal de Salvamento y Seguridad Marítima de Galicia*) confirmed in EuropaPress news how their only rescue helicopter "Helimer" AW139, covering half of Spain's northern coast in the Atlantic, has a minimum of 27 minutes of preparation time in the optimal case before it is cleared for takeoff [5]. A breakdown of this time reveals a standard of 7 minutes for the crew to arrive, a mandatory 15-minute aircraft check, a 5-minute turbine start up, plus the time it may take the airport tower to designate the most immediate available runway.

Furthermore, in July 2020, the Spanish Maritime Salvage (SM, *Salvamento Maritimo*) managed to reduce its response time by a full 30 minutes. A new configuration of the base in Son Sant Joan allowed for the reduction from the previous 45 minutes to the much improved 15-minute response [6]. This was managed by the increase of allocated funds, a change costing 1.3 million annual euros, which allows for practically doubling the base's Helimer crew.

From the previous point it becomes clear how current maritime rescue forces, although evidently effective in their time sensitive labor, could benefit from a much more rapid responding, and cost-efficient operation. One possible solution, object of study of this thesis, is the use of UAVs, more specifically of search and rescue (SAR) drones.

While the use of drones and unmanned vehicles have been around for over two decades, their use have seen an exponential growth over the past years with the technological maturation and government awareness of suitable applications in a wide industry variety. Namely, drones have started to be used in a diverse range of fields such as geographical mapping, crop monitoring, law enforcement, shipping and delivery, disaster management, and of course, SAR missions among others [7].

Many countries have already started employing this advanced technology in the maritime rescue and salvage department. Since June 2021, Spanish SM is using the European Maritime Safety Agency (EMSA) drone CAMCOPTER S100 on the Galician coast with the objective of enhancing general maritime surveillance for tasks such as traffic control and contamination prevention [8]. Furthermore, EMSA also signed a 30-million-euro contract with French companies CLS and Tekever for remotely piloted aircraft surveilling the European waters. The AR5 drone's onboard AI is capable of autonomously detecting survivors and deploying a life raft, calculating the best drop point [5]. Evidently, this supposes a major breakthrough in the field, and will in fact constitute the topic of this thesis.

Figure 1. 2: CAMCOPTER S100 (left) and AR5 (right)

c. Proposed solution and Mission definition

The objective of this thesis is the projection of a rescue UAV similar to the one of EMSA, capable of carrying a life raft as a payload to a specific point in the sea. The mission of this aircraft will be of similar characteristics as the one defined by Gioele Marangoni in his bachelor thesis, *Progettazione preliminare di un UAV ad ala fissa per il soccorso di natanti in panne* [10]. In his thesis, Marangoni emphasized solely on the Central Mediterranean Route, and focusing on the Lampedusa airport as base of operations, identified a working area of 250 km radius. Using this same distance from the Italian *Guardia Costiera* air bases in Catania and Cagliari [11], a complete coverage of this main migration route becomes clear. In addition, this operation area works well too for both Eastern and Western Routes, being these areas big enough to cover the entire Aegean Sea in Greece from any of the Hellenic Guard bases in islands [12], as well as the entire Spanish southern coast from the SM peninsular helicopter bases in Valencia, Almería and Jerez, as well as in the island bases in Palma de Mallorca and Gran Canaria [13]. Map coverage can be seen in the below (Figure 1.3).
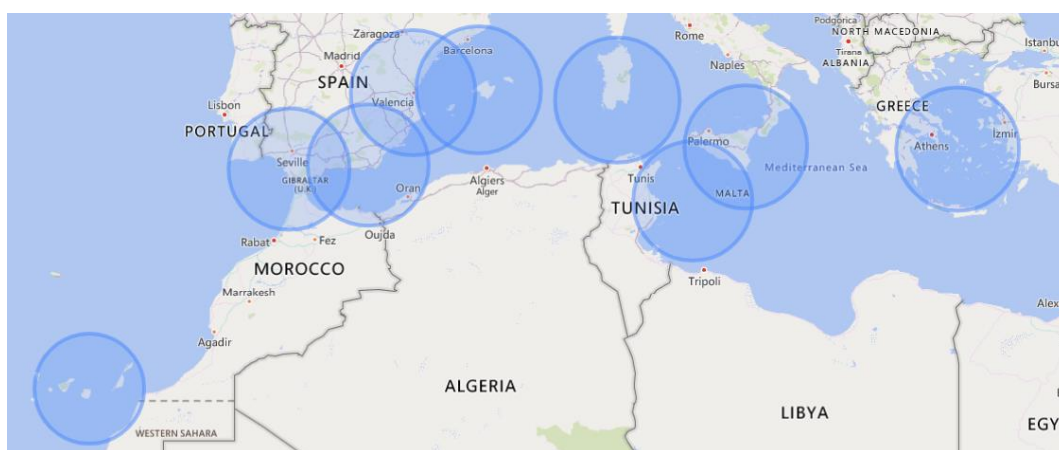

Figure 1. 3: 250 km range from respective coast guard bases

Moreover, Marangoni established a necessary rescue time inferior to 120 minutes, meaning that the UAV must have a cruise speed of 130 km/h: this velocity is more than double than that of SM's boats "*Salvamares*" employed when a rapid response is needed, sailing at speeds of around 30 knots, or 55 km/h [13].

Additionally, another important aspect is the UAV's endurance. Considering then a two-hour cruise post take-off, a maximum loiter time of around two hours for the actual rescue duty of descending from cruise altitude for castaway localization, payload deployment, and climb back to cruise altitude, to then finalize the mission with a two-hour cruise back to base, the drone should have a six-hour autonomy [10].

Lastly, another crucial parameter yet to be defined is the payload. As briefly mentioned, the drone actuation is to, after identifying stranded survivors and a nearby optimal drop point in the sea, release an auto inflatable life raft. The boats in which these migrants travel through the Mediterranean water are often massively overcrowded, well beyond the safety regulations. Due to this issue, the life raft must be big enough to accommodate even the most extreme of situations, and therefore a commercial aviation sized raft could be a suitable solution. One of the biggest of the market, with an overload maximum capability of 84 people EAM Worldwide's EAM-T56 raft [14]. Seeing as it weighs 43.5 kg, this will constitute the UAV's payload [10].

2. Baseline Airfoil Selection
a. Market research and used airfoils

Having defined the mission of the UAV, the next step on the preliminary design of an aircraft is to conduct market research of similar aircraft in order to have a real reference. Marangoni found three similar drones as a model [10], which can be seen in the table 2.1 below:

UAV	Payload (kg)	Cruise velocity (km/h)	Autonomy (h)
Projected	45	130	6
DRS Sentry HP	34	111	8
AR5	50	100	20
Skyrobot FX450	30	125	20

Table 2. 1: Market research

Now, as the first analysis starting point, it is vital to know what the wing configuration is that these different drones employ, specifically the airfoil that each of these aircraft uses. This parameter however is not a simple task to find. Airfoils used by aeronautical manufacturers are proprietary information and are of course not accessible to the public. The AR5 and the FX450 UAVs are the flagships of Tekever and Robot Aviation respectively, and therefore such sensible information has not been found despite performing a thorough search and directly contacting the companies. Thus, further market research must be conducted.

To conduct this research, the airfoil database from the University of Illinois Urbana-Champaign (UIUC) was used [15]. In it, the DRS Sentry HP airfoil was found. A few other UAV aircraft were also listed. Although their mission might not be as similar as the one projected, it will be useful to have in order to perform a comparison. The findings are listed in the table 2.2.

UAV	Payload (kg)	Cruise velocity (km/h)	Autonomy (h)	Airfoil
Projected	45	130	6	-
DRS Sentry HP	34	111	8	NACA 747A315
Aerojet SD-2 MQM-58A	60	560 (max)	0.75	NACA 65A412
TAI Anka-S	200	204	24	NACA 4415
Elbit Skylark 2	10	74 (Skylark 1)	5	Roncz Airfoil
IAI Heron	250	174	52	IAI SA-21
NASA Perseus B	80	96	18	Drela PS-02

Table 2. 2: Airfoils of market research aircraft

The Sentry HP, used by Marangoni in its thesis, began development by the American company DRS Technologies in the 1980s, to then be acquired by DRS in 2002. It mainly

functions as a reconnaissance UAV, mainly performing patrol and observation tasks, being very popular in military applications due to its small size and therefore being difficult to detect by conventional radars. Because of this and its high efficiency, the Sentry HP remains operational [16].

Figure 2. 1: DRS Sentry HP

Aerojet General improved in 1959 a surveillance drone that had been created by the Rheem Manufacturing Co. for the US Army, turning this to be the SD-2/MQM-58A "Overseer". It was built as part of the AN/USD-2 surveillance system, and its payload was easily switchable between missions according to the requirements, such as cameras for real-time photography along with infrared sensors, or equipment tanks for dispensing chemical or biological warfare [17].

Figure 2. 2: Aerojet SD-2/MQM-58A "Overseer"

A more modern project is the one performed by Turkish Aerospace Industries with its ANKA-S, Medium Altitude Long Endurance UAV program. It performed its maiden flight in 2016, entered serial production in 2017, and was first delivered to the Turkish Air Force in 2018. In addition to surveillance and reconnaissance missions, it can also carry out target acquisition and tracking, communication relay, and real-time intelligence among others [18].

Figure 2. 3: TAI Anka-S

These three aircraft airfoil's coordinates have been successfully found in the UIUC Airfoil Data Site and in Airfoil tools. However, research attempts of the other UAVs have been unfortunate, and thus the initial analysis will be carried out simply using the NACA 4415, NACA 65A412 and NACA 747A315 airfoils.

b. Necessary parameters and dimensions

Before continuing with the airfoil analysis, some parameters are to be found. One of the most important ones is the Reynold's number, which is given by the following formula:

$$Re = \frac{\rho\, V\, L}{\mu} \tag{2.1}$$

The Reynolds number used will be the one present in cruise conditions, given that this will be the phase of flight during the majority of the mission. Therefore, the velocity used will be of 130 km/h, or approximately 36.1 m/s. The next needed parameters are density and dynamic viscosity of the air, which both depend on the altitude. Density can be calculated using the Standard Atmosphere ISA model, ISO 2533:1975, which has the following formulas:

$$\rho(h) = 1.225 \left(1 - \frac{6.5 \cdot 10^{-3}\, h}{288.15}\right)^{A-1} \tag{2.2}$$

$$A = \frac{g}{6.5 \cdot 10^{-3}\, R} \tag{2.3}$$

$$g \approx 9.806\ m/s^2 \qquad R = 287\ J/kgK$$

Thus, introducing the 4000 m altitude (and sea level altitude for reference) in (2.2), one obtains the following:

$$\rho(0) = 1.225\ kg/m^3$$
$$\rho(4000) = 0.819\ kg/m^3$$

Then, the dynamic viscosity can be obtained from Sutherland's Law, which is an approximation for how the viscosity of gasses depends on the temperature (which depends on altitude):

$$\frac{\mu}{\mu_0} = \left(\frac{T}{T_0}\right)^{3/2} \frac{T_0 + S_\mu}{T + S_\mu} \tag{2.4}$$

For regular air, the applicable constants are:

$$S_\mu = 111\ K \qquad \mu_0 = 1.716 \cdot 10^{-5}\ N\frac{s}{m^2} \qquad T_0 = 273\ K$$

Temperature at a certain height can also be calculated from the ISA model, equation (2.5). Accordingly, using the cruising (and sea level) altitude, one obtains:

$$T(h) = 288.15 - 6.5 \cdot 10^{-3} h \tag{2.5}$$

$$T(0) = 288.15\ K$$
$$T(4000) = 262.15\ K = -11°C$$

Finally having all values, solving for the viscosity in the Sutherland's Law equation (2.4), one obtains the viscosity, which is subsequently used to find the Reynolds Number:

$$\mu(262.15) = 1.66 \cdot 10^{-6}\ N\, s/m^2$$

Nonetheless, one last parameter remains unknown, dependent on the geometry: the characteristic length. This variable takes many forms, depending on the problem considered.

Within airfoils, it takes the form of the chord. The chord simply consists of the straight line joining the leading and trailing edge, giving the overall length of the airfoil. Specific to this case, the overall aircraft dimension will be taken as the ones found in Marangoni's thesis in his preliminary design, using as reference the market research aircraft.

Marangoni started with the MTOW estimation, which can be decomposed into the payload weight, already defined, and the fuel and empty weights. To calculate the former, he followed the fuel fraction methodology, in which each fuel fraction is calculated iteratively in each of the segments of the mission using Breguet's formulas. The empty weight is then calculated using a simple formula with some tabulated coefficient, with help of DARCorporation's Advanced Aircraft Analysis (AAA) Software. Knowing all contributions, they are added to find the final takeoff weight, $W_{TO} = 1430\ N$ [10].

The next step in the preliminary design is to find the actual dimensions of the projected aircraft. In all design processes, the airplane must follow the restrictions imposed in each of the flight stages by the European Union Aviation Safety Agency. Specifically, those concerning take-off, climb and landing, in addition to some other aerodynamic limitations and cruise speed. Using the AAA software, Marangoni plotted this restriction as curves in the graph confronting the wing loading W_{TO}/S and weight-to-power ratio W_{TO}/P in order to define the possible operating range and select a final design point. Thus, selecting the point with the highest W_{TO}/P from the area complying with the restrictions (as to reduce the required power), and having this coordinate in the graph, the highest W_{TO}/S (to minimize the wing size), Marangoni found a necessary wing surface of $S = 3.5\ m^2$, and selected a wingspan of $b = 5.2\ m$ [10].

As a last step, the Schrenk semiempirical method can be used to calculate the aerodynamic loading and the chord size, as the sum of an Additional aerodynamic load and a Basic aerodynamic load. The former is given by the average between the actual chord distribution and that of an equivalent semi-ellipse wing. The latter is proportional to the twist referred to the zero-lift line direction. Using Matlab to iteratively solve the equations until a desirable result is found, a root chord of $c_{root} = 1.03\ m$ was recovered [10]. This is the value that will be used as the characteristic length for the Reynolds number.

Having now all the necessary parameters, the Reynolds number in which the UAV will operate can be calculated, obtaining:

$$Re = \frac{0.819 \cdot 36.1 \cdot 1.03}{1.66 \cdot 10^{-6}} \approx 1.8 \cdot 10^7$$

c. Airfoil Analysis and Comparison

In this section the three NACA airfoils from the reference market research aircraft will be analyzed and compared to select a base configuration for the projected aircraft. As previously stated, the airfoil coordinates were obtained from the UIUC and Airfoil tools databases.

The three soon to be analyzed airfoils are NACA airfoils, which means that its own name indicates its geometric characteristics. The first digit in the NACA 4415, present in the ANKA-S, describes the maximum camber as a percentage of the chord, the second digit expresses its position as a percentage of the chord from the trailing edge, and the last two digits report the maximum thickness. The NACA 65A412 found in the SD-2/MQM-58A belongs to the 6-series, which has an emphasis on maximizing laminar flow. The first digit after the 6 describes the distance of the minimum pressure area in tenths of the chord. The letter A refers

to a standard profile from an earlier series. The next digit refers to the design lift coefficient in tenths, and the last two depicts again the maximum thickness. Lastly, the NACA 747A315 present in the Sentry HP works similar to the 6-series, but it manages to achieve a further laminar flow maximization by separately identifying the low-pressure zones in the upper and lower surfaces of the airfoil with the first and second digits respectively after the 7 indicating the series. The remaining ones are described the same as with the 6 series.

The analysis will be performed using the open source XFLR5 software, an analysis tool for airfoils, wings and planes operating at low Reynolds Numbers [19]. Table 2.3 summarizes the exact characteristics of the airfoils once introduced into the program, along with the minimum drag coefficient, the maximum lift coefficient, and the point of maximum efficiency. In addition, the polars of the three airfoils are compared side by side. The NACA 4415 can be seen in purple, the NACA 65A412 in blue, and the NACA 747A315 in green.

Profile	Maximum Thickness (%)	Maximum Thickness Position (%)	Maximum Camber (%)	Maximum Camber Position (%)	$C_{d_{min}}$	$C_{l_{max}}$	E_{max}
NACA 4415	15.0	29.3	3.6	42.9	0.0052	2.06	161.2
NACA 65A412	12.0	40.4	2.2	49.9	0.0042	1.95	140.8
NACA 747A315	15.0	39.1	2.5	34.3	0.0034	1.77	128.9

Table 2. 3: Airfoil characteristics

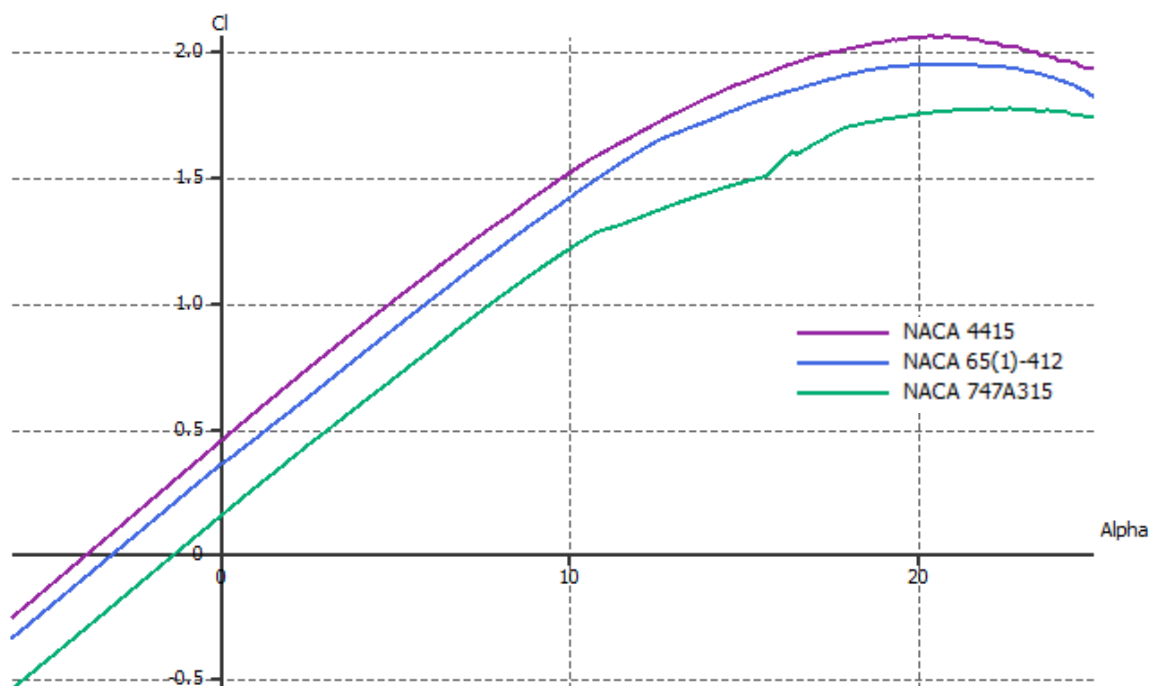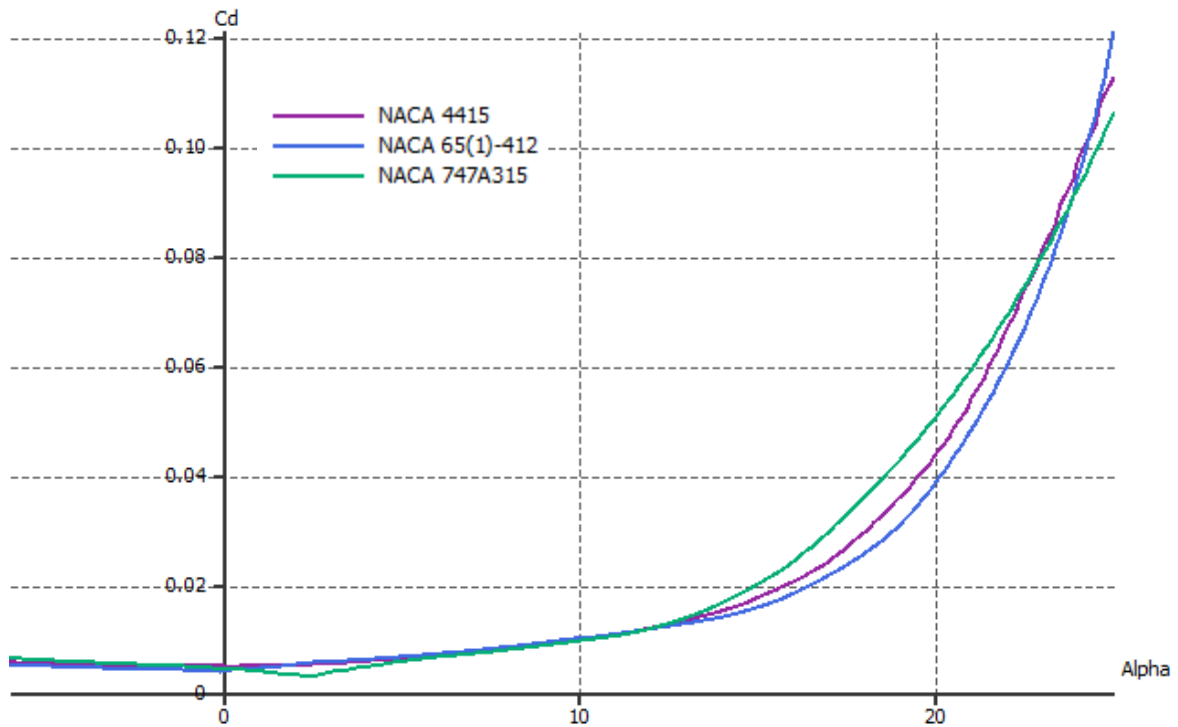*Figure 2. 4: Three airfoil comparison, C_L vs α*

Figure 2. 5: Three airfoil comparison, C_D vs α

As a first analysis it becomes clear that the NACA 4415 seems to offer superior capabilities compared to the other two candidates. From the first graph, C_L vs AoA (Figure 2.5), it is visible that there's a higher lift coefficient for each of the different angles of attack. This behavior is easily attributed to the geometric characteristics, specifically due to the more pronounced thickness and camber of this airfoil. Generally speaking, the thicker and the more cambered the wing is, the more lift it will generate.

Airfoil thickness modifies the overall stall behavior. For thicker airfoils, typically with a value of t/c > 0.15, the flow separation begins at low incidences near the trailing edge, and slowly moves upstream to the trailing edge as α increases. Once the separation point reaches 50%-60% of the chord, the airfoil stalls. Thanks to the higher thickness, there is a smoother variation in the pressure gradient, allowing for a regular development of the flow and thus achieving higher lift values. The following graph (Figure 2.6) compares similar airfoils varying the thickness, in which this effect is clearly seen [20].
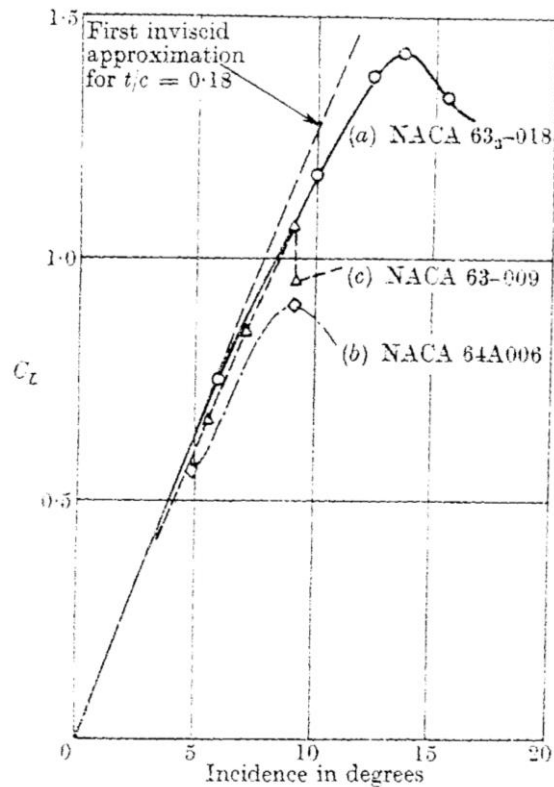
Figure 2. 6: Thickness effect in similar airfoils

Camber is one of the key aspects in lift generation on an airfoil. Increasing the airfoil camber contributes to creating a pronounced differential change in momentum of the flow around the airfoil, causing noticeable differences in pressure between upper and lower airfoil surfaces. This of course creates a significant adverse pressure gradient, and thus substantially a lift increase. This comes with a trade-off of increased drag, as camber also introduces larger flow separation regions. This comes reported in the results of Table 2.3 too, as it can be seen that the NACA 4415 has a higher C_d value.

Perhaps more interestingly, the C_l/C_d graph is also reported (Figure 2.7). It is clear how for a given value of the drag coefficient, the lift coefficient is practically always higher in the NACA 4415 than the other airfoils, except for the minimum C_d values, which occurs at barely null incidence. Additionally, the lift to drag ratio is known as the aerodynamic efficiency, and it is a non-dimensional parameter used to assess the generated aerodynamic forces for efficient flight parameters. The point of maximum efficiency occurs at the incidence angle in which the difference between lift and drag is greatest. However, it is also important to check the point in which this phenomenon occurs. This can be seen in the C_l/C_d vs α graph, seen below. In it, not only the NACA 4415 appears to have an overall higher efficiency, but it is prolonged in a wider range of angles of attack.
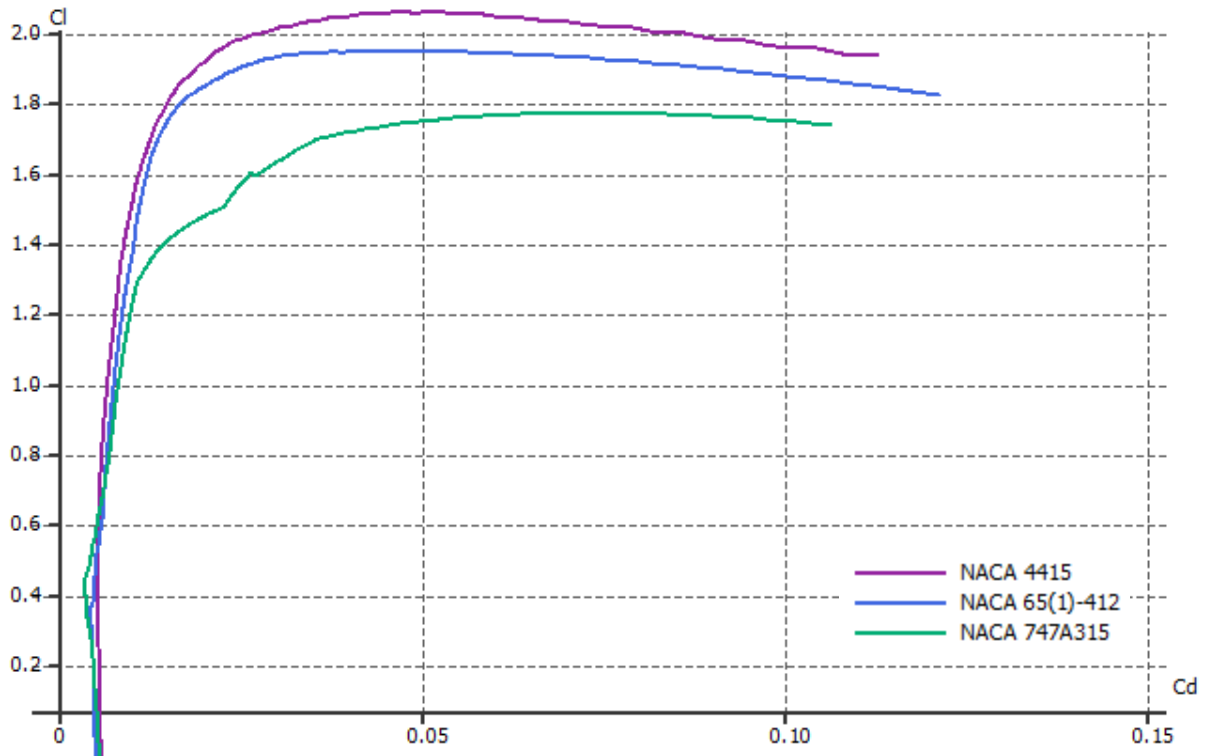
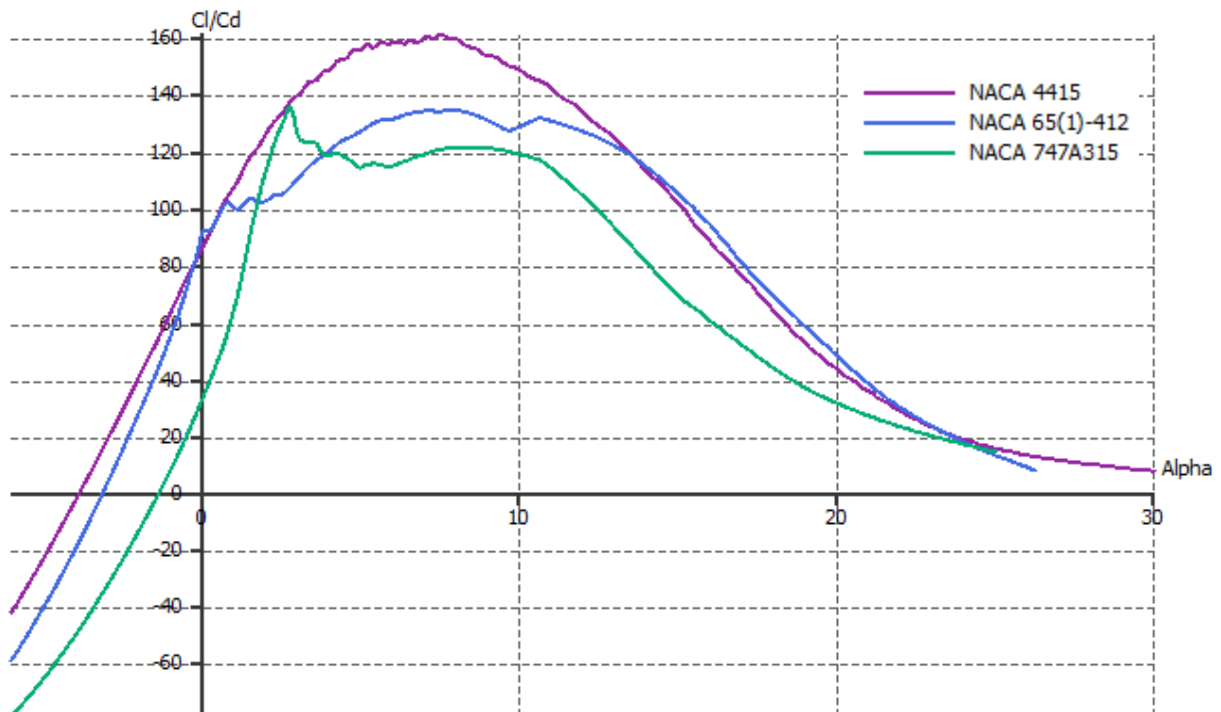*Figure 2. 7: Three airfoil comparison, polar graph*

Figure 2. 8: Three airfoil comparison, efficiency vs α

Having briefly analyzed the behavior of these three airfoils, the better option to select as base configuration appears to be the NACA 4415 airfoil, as it offers an overall better performance, achieving higher lift values for all angles of attack and drag coefficients, thus accomplishing larger aerodynamic efficiency values.

3. Wing Optimization

When converting an infinite, 2D airfoil into a finite span 3D wing, there are many things to consider, and its behavior noticeably differs. The flow over the wing tends to deviate from the tip to the root of the upper surface, while the opposite occurs in the lower surface. This is caused due to the pressure difference between both surfaces, causing the flow to curl around the wrong tips towards the low-pressure region on the upper surface, creating wingtip vortices [21].
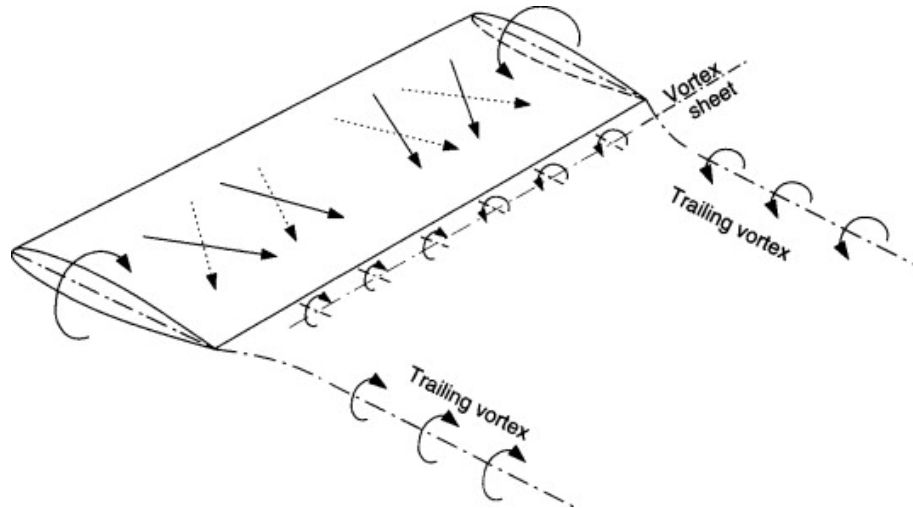

Figure 3. 1: Flow over a finite span wing and vortex system

The vortices formed at the wing tips generate a circulatory motion which trails downstream (Figure 3.1). These disturb the air around, and this motion induces a small downward component of velocity near the wing, called 'downwash'. When combined with the free stream velocity, it generates a local relative wind oriented downwards with an 'induced' angle α_i with respect to V_∞. This downwash has two fundamental consequences; first, the induced angle reduces the angle of attack seen locally by the wing, $\alpha_{ef} = \alpha - \alpha_i$; secondly, the downwash creates and induced drag D_i due to the lift component parallel to V_∞, as the local lift is locally perpendicular to the relative wind. These can be seen in the diagram below (Figure 3.2) [22].
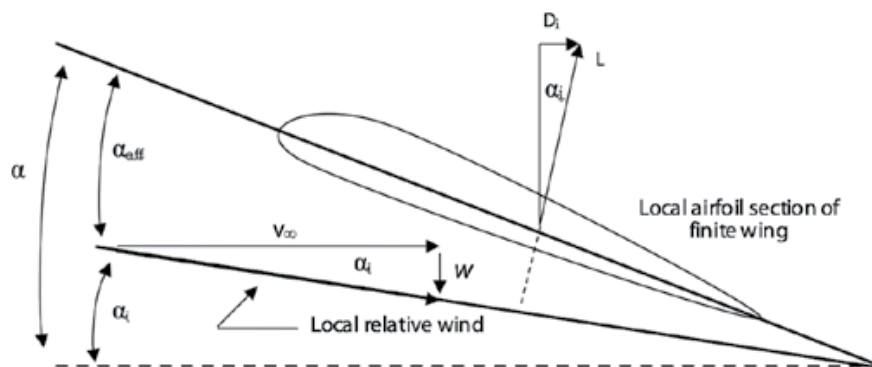

Figure 3. 2: Induced angle of attack and drag

For the finite wing, the total drag coefficient is given by the sum of the parasitic drag coefficient and the induced drag coefficient. Parasite or profile drag is that related to the airfoil polar, which includes the skin friction and form drag, produced by the boundary layer separation and wake. This type of drag is practically unavoidable, and its reduction is not

simple by conventional forms. One possible method is through the stabilization of the laminar boundary layer using distributed suction through small perforations over the wing. This technique in theory delays the flow separation, lowering the skin friction and resulting in a lower drag. In reality, this procedure has quite some obstacles such as high system complexity, delicate manufacturing tolerances and structure, and ineffective surface contamination, among others. A better approach, much more extended and used in modern aviation, is to focus the effort in reducing the induced drag, as its contribution can account for over 50% of overall drag for most subsonic aircraft configurations [23].

The induced drag coefficient can be expressed in function of the lift coefficient, easily identifying its key parameters:

$$C_{D_i} = \frac{C_L^2}{\pi\, e\, AR} \tag{3.1}$$

By maximizing the components of the denominator, the induced drag can be minimized. The wingspan efficiency factor, or Oswald factor e, the aspect ratio AR, and the methods of maximizing them will be explored in the following sections. In addition, further wing performance will be enhanced by the use of the wing twist.

a. Taper ratio

The first variable that is of interest to optimize is the Oswald factor e, which depends entirely in the wing geometry and takes the following form:

$$e = \frac{1}{1 + \delta} \leq 1 \tag{3.2}$$

It is evident from this expression that in order to maximize the induced drag, the wing efficiency factor should be equal to one, meaning that δ needs to be null. This occurs when the aircraft wing has an elliptical planform shape, as the possible values it can assume are given by the elliptic lift distribution. Nonetheless, manufacturing this type of wings is difficult and expensive. A good design compromise is obtained by using instead trapezoidal wings in order to obtain a quasi-elliptic lift distribution, while having a substantially simple manufacture process. For any trapezoidal wing, there is a taper ratio that will minimize the induced drag.

The taper ratio simply is the relation between the wing tip chord and the root chord, as $TR = C_{tip}/C_{root}$. A taper ratio of $TR = 1$ corresponds to a rectangular wing, while a $TR = 0$ means the wing has a triangular shape, as illustrated below in Figure 3.3.
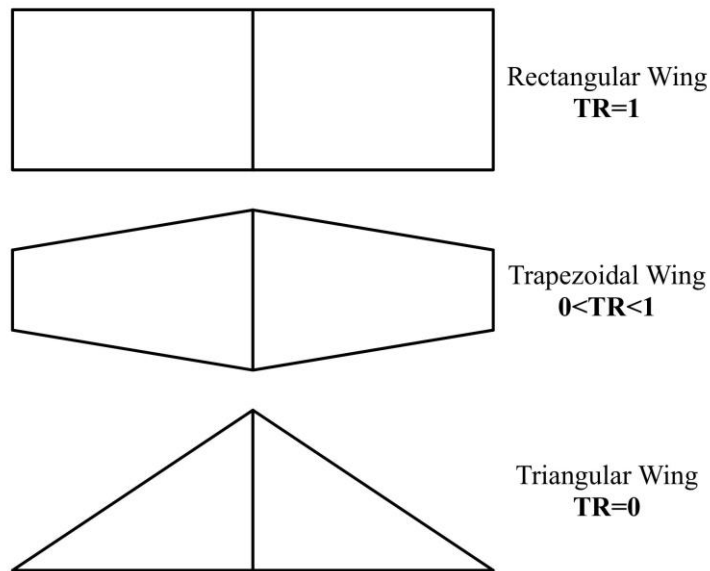
Figure 3. 3: Taper ratio effect

Having already found the values of the wingspan, surface area and the root chord, the taper ratio can easily be found by rearranging the following simple expression:

$$b = \frac{2\,S}{c_{root}\,(1 + TR)} \tag{3.3}$$

$$TR = \frac{2\,S}{c_{root}\,b} - 1 = 0.31$$

This taper ratio means that the chord at the wing tip is $C_{tip} = 0.32$, retaining as previously stated a root chord of $C_{root} = 1.03$.

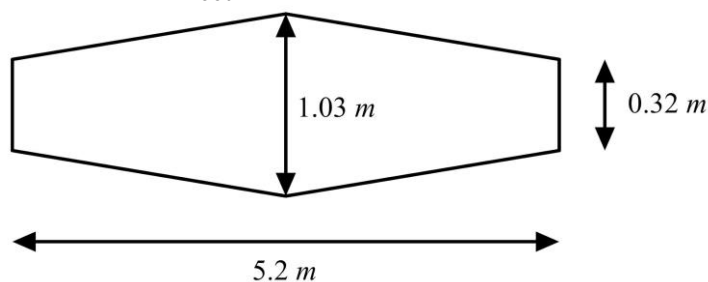

1.03 m   0.32 m

5.2 m

Figure 3. 4: Selected taper and wingspan

b. Aspect ratio

The next factor to consider to minimize the induced drag, considerably more important than the taper ratio, is the aspect ratio, AR. It is the relation between the aircraft's wingspan and its wing surface area, and as previously seen in the induced drag formula it is inversely proportional to it. Because of this, it is always appealing to elevate its value as much as possible. A high AR diminishes the effect of the finite wing, and better approximates that of the infinite wing, normally resulting in a higher lift coefficient, a steeper lift slope, and of course, a reduced induced drag.

Since both the values of the wingspan and surface area are known, the aspect ratio is calculated straightforward:

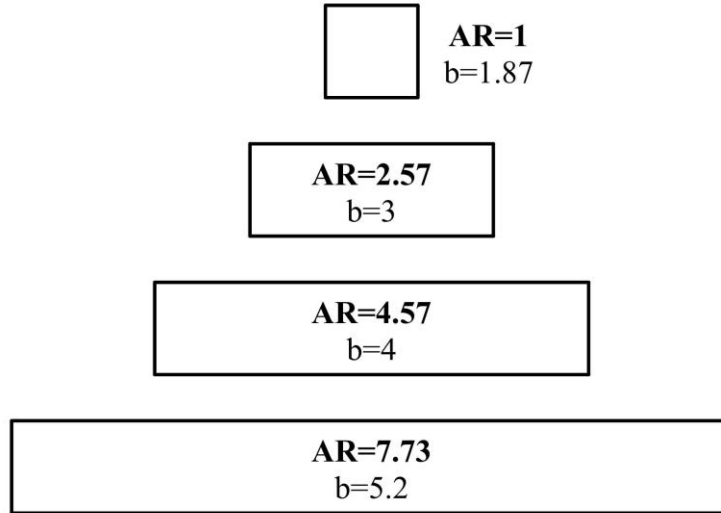$$AR = \frac{b^2}{S} = \frac{5.2^2}{3.5} = 7.73 \tag{3.4}$$

Figure 3. 5: Aspect ratio effect

c. Swept and Dihedral angle

The sweep angle refers to that between the lateral aircraft axis and the wing's quarter-chord line. This typically shows in an aircraft as the wing being angled backwards, although there are some examples of airplanes with a forward sweep. Depending on the chord that is taken as reference, several more sweep angles may be defined. Of particular interest, both the leading and trailing edge can be used to separately define the sweep.

The purpose of introducing a sweep angle to the wing is to delay the compressibility effects that arise when flying at transonic speeds. At these velocities, shockwaves start appearing at a critical Mach number, having a significant effect on the drag. Shockwave direction formation is related to the normal airflow component of the leading edge of a wing section, and not the free stream velocity. By sweeping back the wing, this velocity component can be reduced, which delays the formation of the shockwaves.

Because of this, it would initially seem unnecessary to introduce a sweep angle to the UAV, as its cruising speed is far from the critical Mach speed. Indeed, at the cruising altitude there is a speed of sound of approximately 325 m/s, while the UAV is projected to operate at 36.1 m/s, meaning it will fly at 0.11 Mach, and not at typical critical speeds of around 0.7 – 0.8. Nevertheless, a sweep angle will be introduced since the theory in which the algorithm that will be used to calculate the twist is based assumes a non-zero presence of both trailing and leading edge angles, due to the presence of the taper ratio. Thus, these can be calculated as follows:

$$\Lambda_{LE} = \arctan\left(\frac{c_{root} - c_{tip}}{b}\right) = 7.77^o \tag{3.5}$$

$$\Lambda_{TE} = -\arctan\left(\frac{c_{root} - c_{tip}}{b}\right) = -7.77^o \tag{3.6}$$

Since all input parameters are known, the leading and trailing edge sweep angles are 7.77⁰ and -7.77⁰, so that the wing tip chord is placed centered with respect to the root chord, as seen in Figure 3.6.
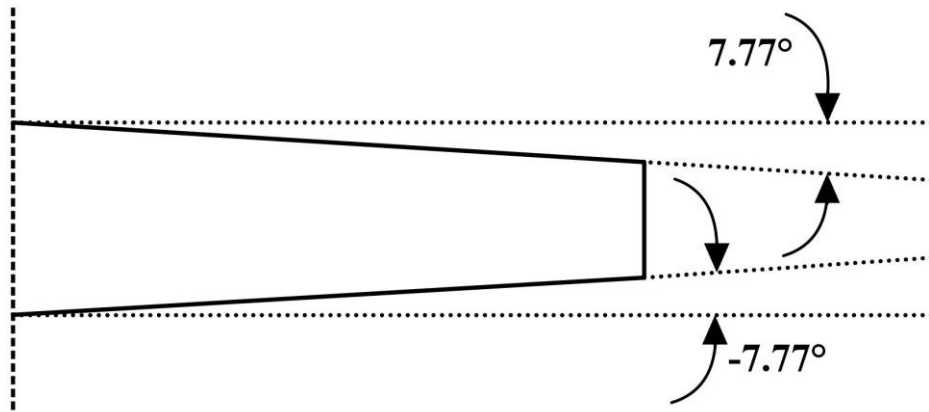
Figure 3. 6: Selected Sweep angle

The dihedral angle refers to the upwards (or less typically downwards, called anhedral) angle formed by the wing and its horizontal. It is used to enhance the aircraft's lateral stability and depending on the configuration it may be used to better accommodate the engines under the wings. However, it negatively affects the lift generation, as it does not produce a completely vertical component, lowers the reference surface area, and it diminishes the roll effectiveness, affecting maneuverability. Because of these reasons, in addition to a harder manufacturability and structural complexity, the dihedral angle will not be used in the UAV.

d. Twist

In this section, an analytical procedure will be implemented in order to find the optimal twist distribution throughout the wingspan, based on Prandtl Lifting-Line theory as described by Professor Phillips' paper from Utah State University [24].

The reason behind introducing a twist angle to the wing is to obtain a lift distribution throughout the wingspan that approximates that of the elliptical wing, which as previously stated, is the one that describes the minimum induced drag. A few noticeable examples of historical aircraft that have used this type of wing are the British Supermarine Spitfire, the American Republic P-47 Thunderbolt and the German Heinkel He 111, all extensively used during the Second World War [25].

23

Figure 3. 7: Spitfire (top left), P-47 Thunderbolt (top right), He 111 (bottom)

Of course, straightly selecting an elliptical wing would be optimal in terms of drag and lift distribution, but immensely impacts the manufacturing aspects and production costs. Because of this, most aircraft throughout history have opted for the approximation throughout the use of the twist. In fact, it can be demonstrated how a tapered wing with optimized twist can achieve the same induced drag coefficient as an elliptical wing, but for a single value of lift coefficient [24]. In the following subsections the formulation, methodology, implantation, and results will be shown.

i. Prandtl's Lifting-Line Theory formulation

The theoretical background in which the twist selection is based is in Prandtl's Lifting-Line theory, as explained by Professor Phillips' paper "Lifting-Line Analysis for Twisted Wings and Washout-Optimized Wings" [24]. For a finite wing with no sweep or dihedral, the foundation of this theory is the following equation:

$$\frac{2\Gamma(z)}{V_\infty c(z)} + \frac{C_{l,\alpha}}{4\pi V_\infty} \int_{-b/2}^{b/2} \frac{1}{z-\zeta}\left(\frac{d\Gamma}{dz}\right)_{z=\zeta} d\zeta = C_{l,\alpha}[\alpha(z) - \alpha_{L0}(z)] \tag{3.7}$$

Once the free-stream velocity V_∞, the geometric and aerodynamic twist $\alpha(z) - \alpha_{L0}(z)$, the planform shape $c(z)$, and the airfoil section lift slope $C_{l,\alpha}$, the only unknown in this equation is the section circulation distribution $\Gamma(z)$.

An analytical solution to Prandtl's Lifting-Line equation can be obtained in terms of a Fourier sine series. From this solution the circulation distribution is given by

$$\Gamma(\theta) = 2\, b\, V_\infty \sum_{n=1}^{\infty} A_n \sin(n\theta) \tag{3.8}$$

in which it can be seen how a new independent variable θ has be used, defined as

$$\theta = \cos^{-1}\left(-\frac{2z}{b}\right) \tag{3.9}$$

and the Fourier coefficients A_n must satisfy the relation

$$\sum_{n=1}^{\infty} A_n \left[1 + n\frac{C_{l,\alpha}\, c(\theta)}{4\, b\, \sin(\theta)}\right] \sin(n\theta) = \frac{C_{l,\alpha}\, c(\theta)[\alpha(z) - \alpha_{L0}(z)]}{4\, b} \tag{3.10}$$

From this circulation distribution, the resulting lift and induced-drag coefficients for the finite wing are found to be

$$C_L = \pi\, AR\, A_1 \tag{3.11}$$

$$C_{D_i} = \pi \, AR \sum_{n=1}^{\infty} n \, A_n^2 = \frac{C_L^2}{\pi \, AR} + \pi \, AR \sum_{n=2}^{\infty} n \, A_n^2 \qquad (3.12)$$

For wings presenting geometric and/or aerodynamic twist, the aerodynamic angle of attack is not constant along the span. Because of this, a practical form of the lifting-line solution can be obtained using the change of variables

$$\alpha(z) - \alpha_{L0}(z) \equiv (\alpha - \alpha_{L0})_{root} - \Omega \, \omega(\theta) \qquad (3.13)$$

where Ω is defined to be the maximum total washout, geometric and aerodynamic,

$$\Omega \equiv (\alpha - \alpha_{L0})_{root} - (\alpha - \alpha_{L0})_{max} \qquad (3.14)$$

and ω is the washout distribution normalized with respect to the maximum total washout:

$$\omega(\theta) \equiv \frac{\alpha(\theta) - \alpha_{L0}(\theta) - (\alpha - \alpha_{L0})_{root}}{(\alpha - \alpha_{L0})_{max} - (\alpha - \alpha_{L0})_{root}} \qquad (3.15)$$

Introducing equation (3.13) in (3.10) results in

$$\sum_{n=1}^{\infty} A_n \left[1 + n \frac{C_{l,\alpha} \, c(\theta)}{4 \, b \sin(\theta)} \right] \sin(n\theta) = \frac{C_{l,\alpha} \, c(\theta)}{4 \, b} [(\alpha - \alpha_{L0})_{root} - \Omega \, \omega(\theta)] \qquad (3.16)$$

in which the Fourier coefficient A_n can be written as

$$A_n \equiv a_n (\alpha - \alpha_{L0})_{root} - b_n \Omega \qquad (3.17)$$

where the Fourier coefficients a_n and b_n are obtained from

$$\sum_{n=1}^{\infty} a_n \left[\frac{4 \, b}{C_{l,\alpha} \, c(\theta)} + \frac{n}{\sin(\theta)} \right] \sin(n\theta) = 1 \qquad (3.18)$$

$$\sum_{n=1}^{\infty} b_n \left[\frac{4 \, b}{C_{l,\alpha} \, c(\theta)} + \frac{n}{\sin(\theta)} \right] \sin(n\theta) = \omega(\theta) \qquad (3.19)$$

The coefficients a_n and b_n represent the contribution of the planform and the twist respectively at infinite coefficients A_n, which in turn defines the solution to the lifting line equation.

Introducing equation (3.17) in equations (3.11) and (3.12), the lift and induced drag coefficients can be expressed as:

$$C_L = \pi \, AR \, A_1 = \pi \, AR \, [a_1 (\alpha - \alpha_{L0})_{root} - b_1 \Omega] \qquad (3.20)$$

$$C_{D_i} = \frac{C_L^2}{\pi \, AR} + \pi \, AR \sum_{n=2}^{\infty} n \, [a_n^2 (\alpha - \alpha_{L0})_{root}^2 - 2 \, a_n \, b_n (\alpha - \alpha_{L0})_{root} \Omega + b_n^2 \Omega^2] \qquad (3.21)$$

which can be rearranged algebraically to yield

$$C_L = C_{L,\alpha} \, [(\alpha - \alpha_{L0})_{root} - \Omega \varepsilon_\Omega] \qquad (3.22)$$

$$C_{D_i} = \frac{C_L^2 (1 + k_D) - k_{DL} C_L C_{L,\alpha} \Omega + k_{D\Omega} (C_{L,\alpha} \Omega)^2}{\pi \, AR} \qquad (3.23)$$

where its components are defined as:

$$C_{L,\alpha} = \pi \, AR \, a_1 = \frac{C_{l,\alpha}}{\left(1 + \frac{C_{l,\alpha}}{\pi \, AR} \right) (1 + k_L)} \qquad (3.24)$$

$$k_L = \frac{1 - \left(1 + \frac{\pi\,AR}{C_{l,\alpha}}\right)a_1}{\left(1 + \frac{\pi\,AR}{C_{l,\alpha}}\right)a_1} \tag{3.25}$$

$$\varepsilon_\Omega = \frac{b_1}{a_1} \tag{3.26}$$

$$k_D = \sum_{n=2}^{\infty} n\frac{a_n^2}{a_1^2} \tag{3.27}$$

$$k_{DL} = 2\frac{b_1}{a_1}\sum_{n=2}^{\infty} n\frac{a_n}{a_1}\left(\frac{b_n}{b_1} - \frac{a_n}{a_1}\right) \tag{3.28}$$

$$k_{D\Omega} = \left(\frac{b_1}{a_1}\right)^2\sum_{n=2}^{\infty} n\left(\frac{b_n}{b_1} - \frac{a_n}{a_1}\right)^2 \tag{3.29}$$

These respectively represent the airfoil section lift slope for the finite wing (3.24), a coefficient relating to the lift slope (3.25), the twist effectiveness (3.26), a coefficient relating to the planform contribution to the induced drag (3.27), a coefficient relating to the contribution of the lift and twist to induced drag (3.28), and one last coefficient relating to the contribution to only the twist to the induced drag (3.29).

Differentiating the induced drag equation (3.23) with respect to the total washout at a constant lift coefficient, it can be seen that the minimum drag is obtained for any given planform shape $c(z)$, any washout distribution $\Omega(z)$, and any design lift coefficient $C_{L,d}$, by using an optimal washout Ω_{opt} given by

$$C_{L,\alpha}\Omega_{opt} = \frac{k_{DL}\,C_{Ld}}{2\,k_{D\Omega}} \tag{3.30}$$

From this equation it can be checked how for an elliptical wing there is no need of washout, as it is already optimized since for these wings k_{DL} is zero. Furthermore, using the optimal washout from equation (3.30) in the induced drag (3.24), it is possible to find the induced drag coefficient for a wing of an arbitrary planform, given by

$$(C_{D_i})_{opt} = \frac{C_L^2}{\pi\,AR}\left[1 + k_D - \frac{k_{DL}^2}{4\,k_{D\Omega}}\left(2 - \frac{C_{Ld}}{C_L}\right)\frac{C_{Ld}}{C_L}\right] \tag{3.31}$$

From this expression, the fact that an optimized wing with a twist will always produce less drag than one that is not with the same dimension, is clearly identifiable. In addition, if the actual lift coefficient used is equal to the design lift coefficient, equation (3.31) reduces to

$$(C_{D_i})_{opt} = \frac{C_L^2}{\pi\,AR}(1 + k_{Do}) \tag{3.32}$$

in which

$$k_{Do} = k_D - \frac{k_{DL}^2}{4\,k_{D\Omega}} \tag{3.33}$$

Equation (3.33) defines what is the optimal factor of induced resistance, which is again zero for an elliptical wing, being both k_{DL} and k_D null. This optimal value can also be achieved for non elliptical wings by means of a combination of a linear variation of the chord in the spanwise direction $c(\theta)$ and a twist function $\omega(\theta)$:

$$c(\theta) = \frac{2\,b}{AR\,(1+TR)}[1 - (1-TR)|\cos(\theta)|] \tag{3.34}$$

$$\omega(\theta) = 1 - \frac{\sin(\theta)}{1 - (1-TR)|\cos(\theta)|} \tag{3.35}$$

In this way, any wing of arbitrary planform that satisfies these equations and operating at the design lift coefficient will have the same minimum induced drag coefficient of that of an elliptical wing of equivalent dimensions.

Introducing equations (3.34) and (3.35) into (3.18) and (3.19), the following is obtained:

$$\sum_{n=1}^{\infty} \frac{a_n}{a_1}\sin(n\theta) + \frac{C_{l,\alpha}[1-(1-TR)|\cos(\theta)|]}{2\,AR\,(1+TR)} \sum_{n=1}^{\infty} n\frac{a_n}{a_1}\frac{\sin(n\theta)}{\sin(\theta)} = \frac{C_{l,\alpha}[1-(1-TR)|\cos(\theta)|]}{2\,a_1 AR\,(1+TR)} \tag{3.36}$$

$$\sum_{n=1}^{\infty} \frac{b_n}{b_1}\sin(n\theta) + \frac{C_{l,\alpha}[1-(1-TR)|\cos(\theta)|]}{2\,AR\,(1+TR)} \sum_{n=1}^{\infty} n\frac{b_n}{b_1}\frac{\sin(n\theta)}{\sin(\theta)} = \frac{C_{l,\alpha}[1-(1-TR)|\cos(\theta)|]}{2\,b_1 AR\,(1+TR)} \tag{3.37}$$

In order to obtain the various a_n coefficients, it is necessary to truncate the series expansion to the N-th order, that is, using equation (3.36) in correspondence with N sections of the wing along the span, with the first and last sections located in the wingtips, and the intermediate sections equally spaced in θ. This results in the need of solving a NxN algebraic system, defined as:

$$\sum_{n=1}^{\infty} \frac{a_n}{a_1}\sin(n\theta_i) + \frac{C_{l,\alpha}[1-(1-TR)|\cos(\theta_i)|]}{2\,AR\,(1+TR)} \sum_{n=1}^{\infty} n\frac{a_n}{a_1}\frac{\sin(n\theta_i)}{\sin(\theta_i)} = \frac{C_{l,\alpha}[1-(1-TR)|\cos(\theta_i)|]}{2\,a_1 AR\,(1+TR)} \tag{3.38}$$

in which

$$\theta_i = \frac{(i-1)\pi}{N-1}, \quad i = 1, \dots, N \tag{3.39}$$

It is important to draw attention to the wingtips, at $\theta = 0$ and $\theta = \pi$, in which there are singularities than can be solved imposing

$$\left[\frac{\sin(n\theta)}{\sin(\theta)}\right]_{\theta \to 0} = n \qquad \left[\frac{\sin(n\theta)}{\sin(\theta)}\right]_{\theta \to \pi} = (-1)^{n+1}n \tag{3.40}$$

A completely analogous process can be followed in order to find the other b_n coefficients in equation (3.37), or through a Fourier series expansion and trigonometric relations it can be proven that

$$b_n = \begin{cases} a_1 - (1-a_1)\dfrac{C_{l,\alpha}}{2\,AR\,(1+TR)}, & for\ n = 1 \\[2mm] a_n\left[1 + \dfrac{C_{l,\alpha}}{2\,AR\,(1+TR)}\right], & for\ n \neq 1 \end{cases} \tag{3.41}$$

Therefore, using the result found in (3.41), and inserting equations (3.24) and (3.27) into (3.28) and (3.29), it is found that for a wing with linear taper and optimal twist defined from (3.35), the coefficients relating to lift and twist can be rewritten to

$$k_{DL} = \frac{\pi C_{l,\alpha}}{(1+TR)C_{L,\alpha}}k_D \tag{3.42}$$

$$k_{D\Omega} = \left(\frac{\pi C_{l,\alpha}}{(1+TR)C_{L,\alpha}}k_D\right)^2 \tag{3.43}$$

And from these last equations, the final equation for the induced drag coefficient produced by any given wing results in

$$C_{D_i} = \frac{C_L^2}{\pi \, AR} + \frac{k_D}{\pi AR}\left[C_L - \frac{\Omega \, \pi \, C_{l,\alpha}}{2(1+TR)}\right]^2 \tag{3.44}$$

In order to minimize the induced drag coefficient and make it equal to that of an elliptical wing with the same geometric characteristics, producing the same design lift coefficient but without the twist, an expression for the maximum washout can be found:

$$\Omega_{opt} = \frac{2(1+TR)\,C_{Ld}}{\pi \, C_{l,\alpha}} \tag{3.45}$$

This twist expression, along with the proper design lift coefficient, will cancel the entire second term from the induced drag coefficient, thus making it minimal and equal to that of the elliptical wing, as seen in equation (3.1) with an Oswald factor of unitary value. The design lift coefficient will be selected as the one needed for cruise conditions, as this is the phase of the mission in which the UAV will operate the majority of the time and therefore it is of interest to reduce the drag generated in it. Hence, during cruise the total lift must be equal to that of the UAV weight, and so the lift coefficient can be found using the following expression:

$$C_{Ld} = \frac{W_{TO}}{\frac{1}{2}\rho V_\infty^2 S} \tag{3.46}$$

Ultimately, all needed equations and parameters have been developed and it can be proceeded with their actual calculus with software help.

ii. Twist calculation using Matlab

This section will deal with the calculation of all the needed variables and parameters introduced by Prandtl's Lifting-Line theory, explained in detail in the previous section, with help of the Matlab software. In addition to the previously calculated parameters, the first step is to calculate the design lift coefficient using equation (3.46), which results in $C_{Ld} = 0.77$. This can now subsequently be used to find the maximum washout angle using (3.45), and assuming a value for the lift slope of $C_{l,\alpha} = 2\pi$, results in optimal total maximum twist of $\Omega_{opt} = 5.82°$. Lastly, the zero lift angle of the NACA 4415 is needed, which is obtained from the XFLR5 airfoil analysis, resulting in $\alpha_{L0} = -3.875°$.

Upcoming, the Matlab code in which the series expansion Fourier coefficients truncated to the 1000-th order is reported. This code was used by Mangiantini in his master degree Thesis "*Design parametrico di un'ala di un UAV e stima delle prestazioni attraverso prove di volo con un prototipo in scala*" [26]. It has been adapted and used to calculate the distribution of the induced drag coefficient as a function of the lift coefficient in addition to twist distribution along the wingspan. Throughout the code, comments are placed to point out the several equations used.

```matlab
%% Induced drag coefficient for the optimized wing
N= 1000;
S= 3.5; %[m^2]
AR= 7.73;
TR= 0.31;
Cla= 2*pi; %[1/rad]
span= 5.2;%[m]
altitude= 4000; %[m]
g= 9.807; %[m/s^2]
```

```matlab
R= 287; %[J/kg K]

rho=1.225*(1-(6.5*10^(-3)*altitude)/288.15)^((g/(6.5*10^(-3)*R))-
1); %[kg/m^3]
Cld= 1430/(0.5*rho*36.1^2*S);
a_al0root=linspace(0,10,100)*pi/180;
maxtotwash= (2*(1+TR)*Cld)/(pi*Cla); %[rad]
maxtowash_deg = rad2deg((2*(1+TR)*Cld)/(pi*Cla));

% Vector definition of the new independent variable theta eq.(3.39)
thetha= linspace(0,pi,N);

% Chord length throughout the wingspan eq.(3.34)
for i=1:length(thetha)
    c(i)= 2*span / (AR *(1+TR)) *(1 - (1-TR)*abs(cos(thetha(i))));
end

% Calculus of the Fourier series coefficient an and bn
% Matrix construction of the coefficients of the algebraic system M(NxN)
% eq.(3.38)e(3.40)
for i=2:N-1
    for n=1:N
        M(I,n)=sin(n*thetha(i))+ n * Cla*(1-(1-
TR)*abs(cos(thetha(i))))/(2*AR*(1+TR))*sin(n*thetha(i))/sin(thetha(i));
    end
    rhs(i)= Cla*(1-(1-TR)*abs(cos(thetha(i))))/(2*AR*(1+TR));
end
for n=1:N
    M(1,n)= n^2 * Cla*(1-(1-TR)*abs(cos(thetha(i))))/(2*AR*(1+TR));
    M(N,n)= ((-1)^(n+1))*n^2*Cla*(1-(1-
TR)*abs(cos(thetha(i))))/(2*AR*(1+TR));
end
rhs(1)= Cla*(1-(1-TR))/(2*AR*(1+TR));
rhs(N)= Cla*(1-(1-TR))/(2*AR*(1+TR));

% Algebraic system solution Mxa'=rhs'
a=zeros(N,1);
a=inv(M)*rhs';

% bn coefficient calculation from the an eq.(3.41)
b=zeros(N,1);
b(1)=a(1)-((1-a(1))*Cla/(2*AR*(1+TR)));
for n=2:N
    b(n)=a(n)*(1+(Cla/(2*AR*(1+TR))));
end
% Effectiveness eq.(3.26)
effectiveness=b(1)/a(1);

% KL eq.(3.25)
KL= (1-(1+(pi*AR/Cla))*a(1))/((1+(pi*AR/Cla))*a(1));

% Finite wing lift curve slope eq.(3.24)
Cla= Cla/ ( (1 +(Cla/pi/AR))*(1+KL));

% KD eq.(3.27)
for nn= 2:N
    KDtmp(nn)= nn * a(nn)^2/a(1)^2;
end
KD=sum(KDtmp);
```

```
% KDL eq.(3.42)
KDL= (pi*Cla*KD) / ((1+TR)*Cla);


% Kdomega eq. (3.43)
Kdomega= ((pi*Cla) / (2*(1+TR)*Cla))^2 * KD;


% Finite wing lift coefficient eq.(3.22)
CL=Cla*((a_al0root-effectiveness*maxtotwash));


% Induced drag coeeficient eq.(3.44)
Cdi= CL.^2 / (pi*AR) + KD/(pi*AR)* ( CL -
( (pi*Cla*maxtotwash)/(2*(1+TR)))).^2;


%% Optimal twist distribution
% Aerodynamic incidence to generate at the root CLd
a_al0rootCld=(Cld/Cla+effectiveness*maxtotwash);


% Geometric incidence at root assuming NACA 4415 (alphaL0=-3.875°)
arooth=(a_al0rootCld)*180/pi-3.875;


% Vector definition of the independent variable z
z=linspace(-span/2,span/2,1000);


% Distribution of the optimal dimensionless twist along z
% eq.(3.9)e(3.35)
w= 1-(sqrt(1-(2*z/span).^2))./(1-(1-TR)*abs(2*z/span));


% Optimal twist along the wingspan eq.(3.13)
a_al0=a_al0rootCld*180/pi-maxtotwash*w*180/pi;
```


The first ten lines of the algorithm are the input parameters that will then be used by the algorithm to calculate the desired ones. This consist of, in order, the N number of sections in which the wings are discretized, the reference surface area S, the calculated aspect ratio AR and taper ratio TR, the assumed lift slope coefficient $C_{l,\alpha}$, the chosen cruising altitude, and the gravity constant g and ideal gas constant R.

iii.   Twist results

Varying the input arguments affecting the induced drag coefficient, it is compelling to see the impact these have directly on it, as explained theoretically in earlier sections. Specifically, the two parameters of interest are the first two defined under section 3 of this work, that is the taper ratio and the aspect ratio.

From equation (3.44) it can be seen how the aspect ratio is inversely proportional to the induced drag coefficient, meaning that bigger values of the AR will minimize the drag. The TR also helps to diminish the drag; smaller values of TR will maximize the value of the fraction which is subtracted from the drag contribution. Therefore, by analyzing a series of wings of identical dimensions, only varying the parameter in question, it can be seen how maximizing the AR and minimizing the TR has a positive effect on the overall induced drag coefficient. The results of these two analyses can be seen in the two following graphs, Figures 3.8 and 3.9.
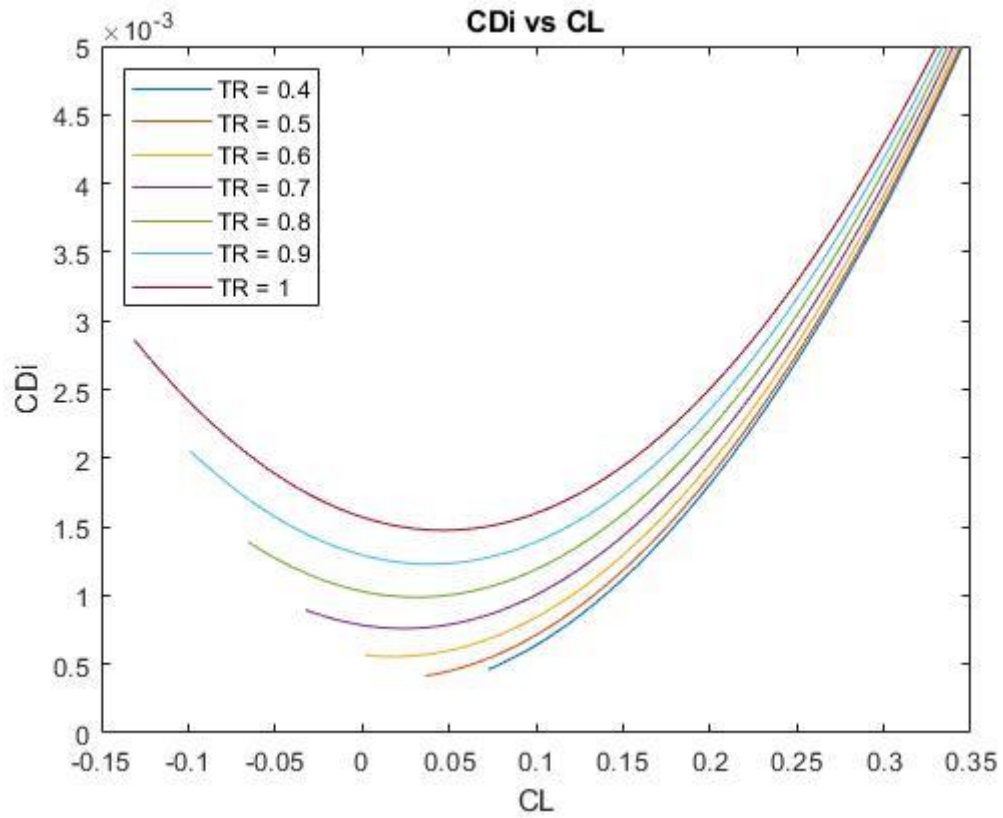
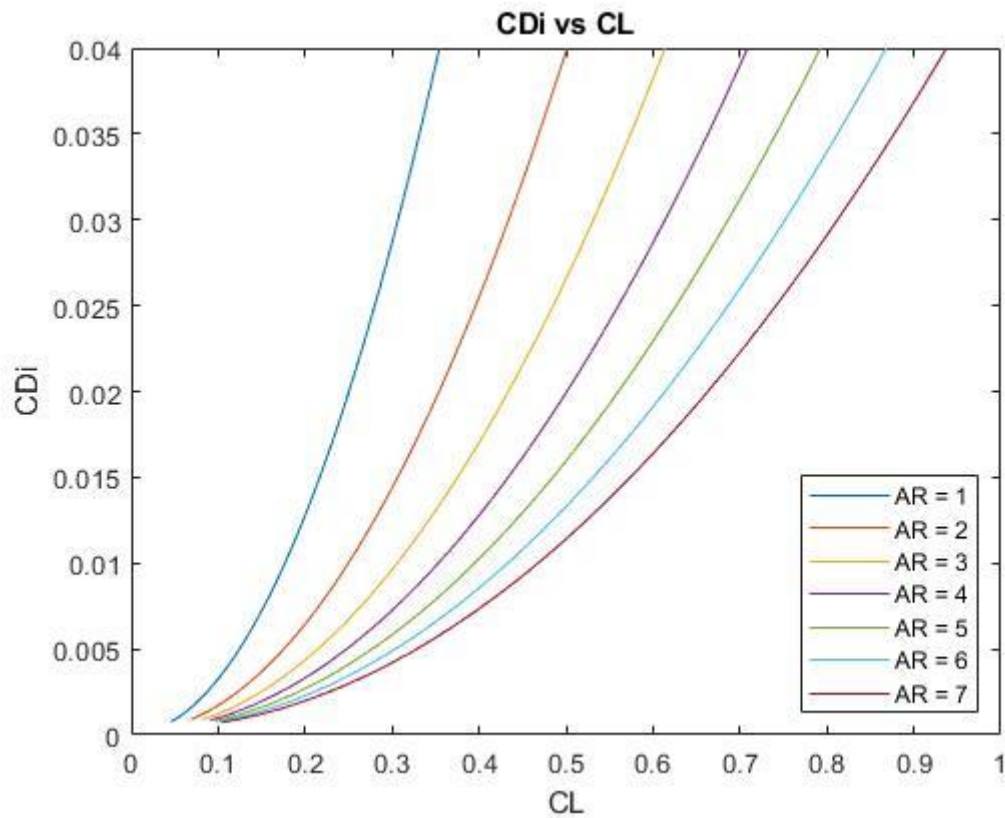*Figure 3. 8: Taper Ratio effect on induced drag*

Figure 3. 9: Aspect Ratio effect on induced drag

Furthermore, using the optimal twist distribution throughout the wingspan found with equation (3.13) the base wing and the ideal wing design can be compared to see the actual improvement quantitatively. The base wing consists of the same chord and surface area, adjusting the wingspan to account for the absence of taper to use a rectangular planform. The geometric characteristics of these can be checked in the following table 3.1:

Parameter	Base wing	Optimized Wing
Airfoil	NACA 4415	
Lift slope $C_{l,\alpha}$	2π	
Surface Area S	3.50 m^2	
Wingspan b	3.40 m	5.20 m
Aspect Ratio AR	3.30	7.73
Taper ratio TR	1	0.31
Optimal Twist $\alpha(z) - \alpha_{L0}(z)$	Not applied	Applied

Table 3. 1: Characteristics of the base and optimized wings

Likewise, the following graphs the confrontation of both wings on induced drag coefficient (Figure 3.10), and the applied twist distribution on the optimized wing (Figure 3.11).
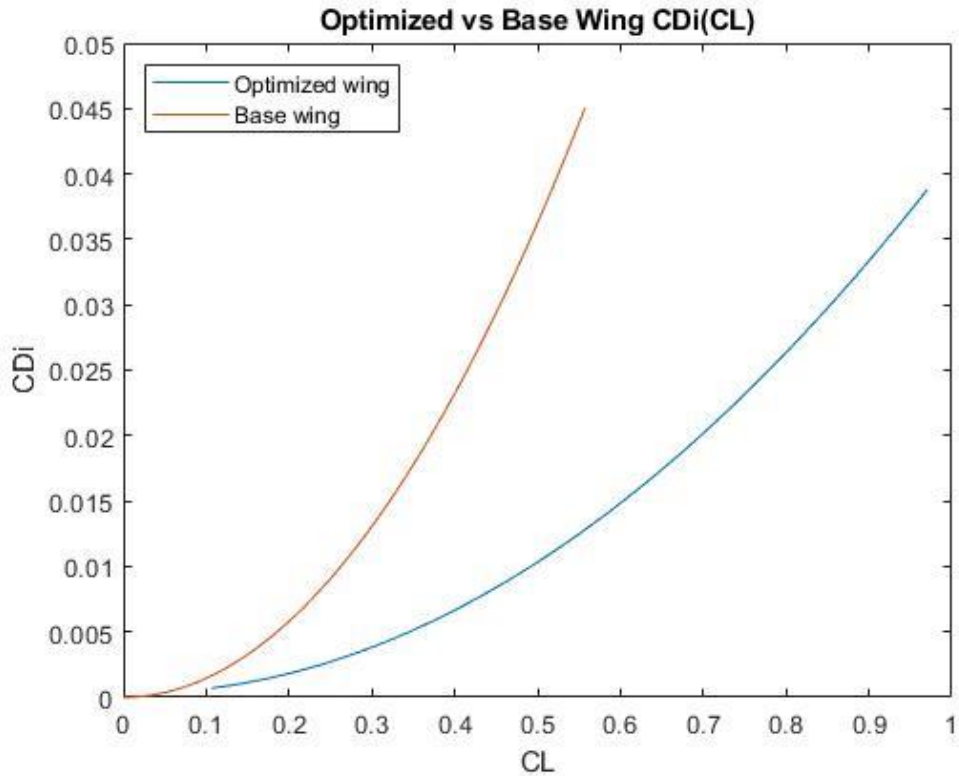
Figure 3. 10: Induced drag comparison between base and optimized wing
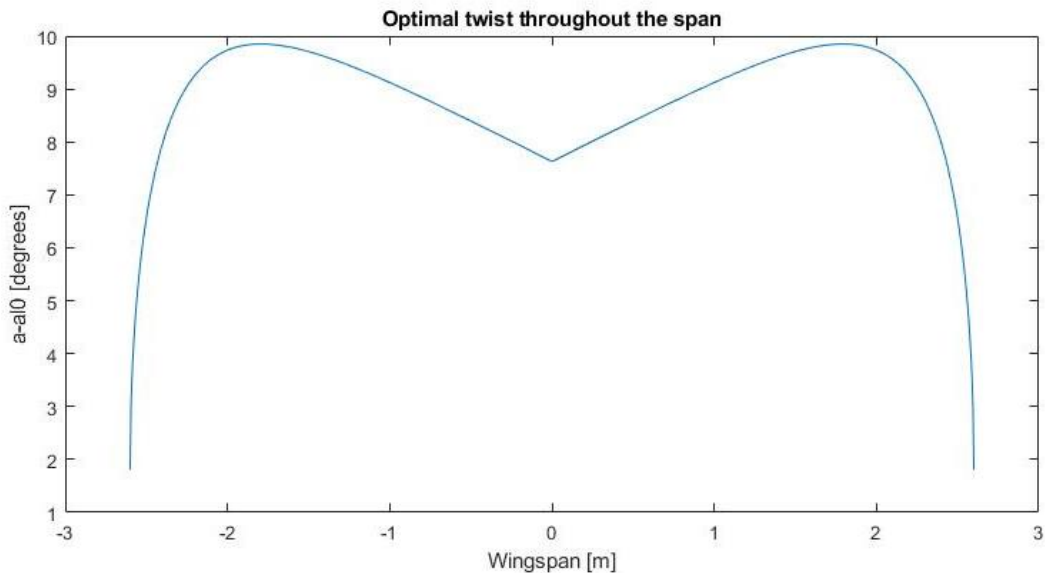

Figure 3. 11: Recovered optimal twist distribution throughout the span

It becomes immediately clear that the optimized wing manages to substantially reduce the induced drag coefficient for each and every value of the lift coefficient. A numerical result can further be obtained by comparing its value at the design lift coefficient. At this point, the equivalent drag induced of the optimized and base wing are 0.024 and 0.085, which translate into a reduction of 71.62% with respect to the starting case in cruise conditions, for the same wing surface area thanks to the taper ratio introduction, aspect ratio enlargement and twist implementation.

iv.   Final wing design

Having found the optimal twist throughout the aircraft's span, it is now possible to combine all of the calculated parameters into a single design. The twist angle will be applied through a geometric twist as to not change the already selected airfoil. Therefore, the NACA 4415 will be rotated from the trailing edge as specified from the graph in the previous section. For visualization purposes, the wing will be created in the design software Autodesk Fusion 360 by adjusting the airfoil accordingly each tenth of the chord until 90% of its length, from which it will then be adjusted at more frequent percentages due to the rapid change in angle. Each rotation can be seen in the table 3.2:

Chord (respective to tip)	Chord length (m)	Geometric angle (degrees)
Root	1.030	7.638
0.10	0.959	8.028
0.20	0.888	8.424
0.30	0.817	8.890
0.40	0.746	9.176
0.50	0.675	9.504
0.60	0.604	9.754
0.70	0.533	9.848
0.80	0.462	9.604
0.90	0.391	8.502
0.95	0.356	7.083
0.97	0.341	6.086
0.98	0.334	5.384
0.99	0.327	4.398
Tip	0.320	1.806

Table 3. 2: Chord length and angle throughout the wingspan

The actual airfoil placement can be created now. These are created, scaled, and rotated according to the table. Then, a simple Loft operation is performed, which smoothly creates a body between the given profiles. This will create the design semi-wing. The entire wing can be created by mirroring the body by the root plane. Results are seen in Figure 3.12.
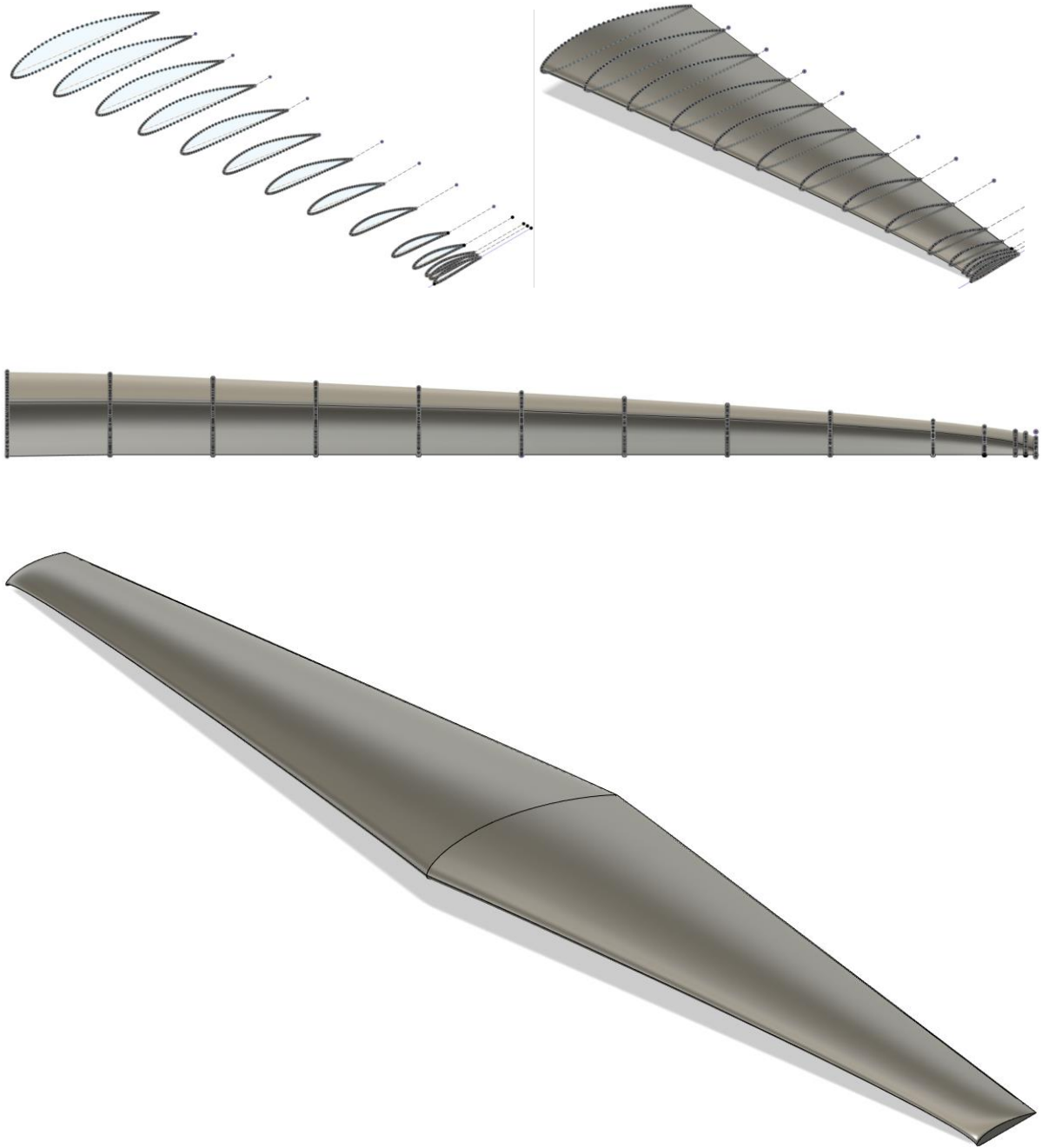
Figure 3. 12: Different views of the designed optimized wing

4. Optimized wing comparison with the base configuration

This final thesis section will compare the newly designed optimized wing with the base wing. That is, the wing resulting from using the same airfoil with the same surface area and root chord, while keeping it rectangular and twistless, as previously mentioned. So, taking these specifications into account, both wings are modeled in XFLR5 by defining intermediate airfoils. It is simpler in the base wing, since there is no airfoil variation along the wingspan, it can be modeled only by specifying the wingtip and the root. In the optimized case however, the airfoil has been updated at several points throughout the span, changing the scale, the position, and the twist, as done in the previous section. In the figure below both wings can be seen (Figure 4.1): the starting wing can be seen in yellow, while the optimized wing is seen in blue.
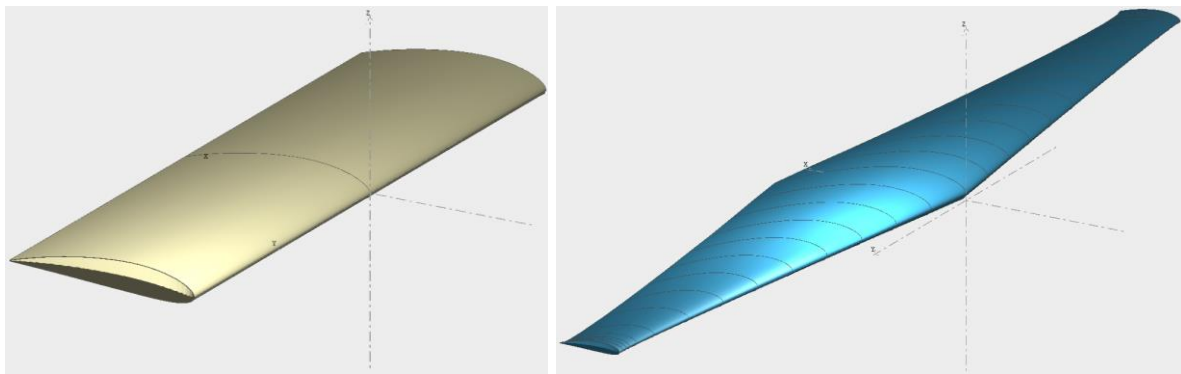

Figure 4. 1: Base wing (left) and optimized wing (right)

Now that the models are ready, it is possible to perform the analysis. Setting the correct parameters and running the program, similar to how was procedure in the airfoil analysis, the polars can be obtained. The first graph that is interesting to analyze is the polar curves: below, the drag against the lift coefficients can be seen (Figure 4.2). It is clear that the new design, seen in blue, achieves much smaller C_D values through the C_L range without exceptions when compared against the base wing, seen in orange. Looking only at the lift coefficient against the angle of attack (Figure 4.3), a substantial improvement can be observed as well. Throughout the entire α range, the optimized wing achieves superior lift values, with an almost constant difference of an entire unit of value among wings.
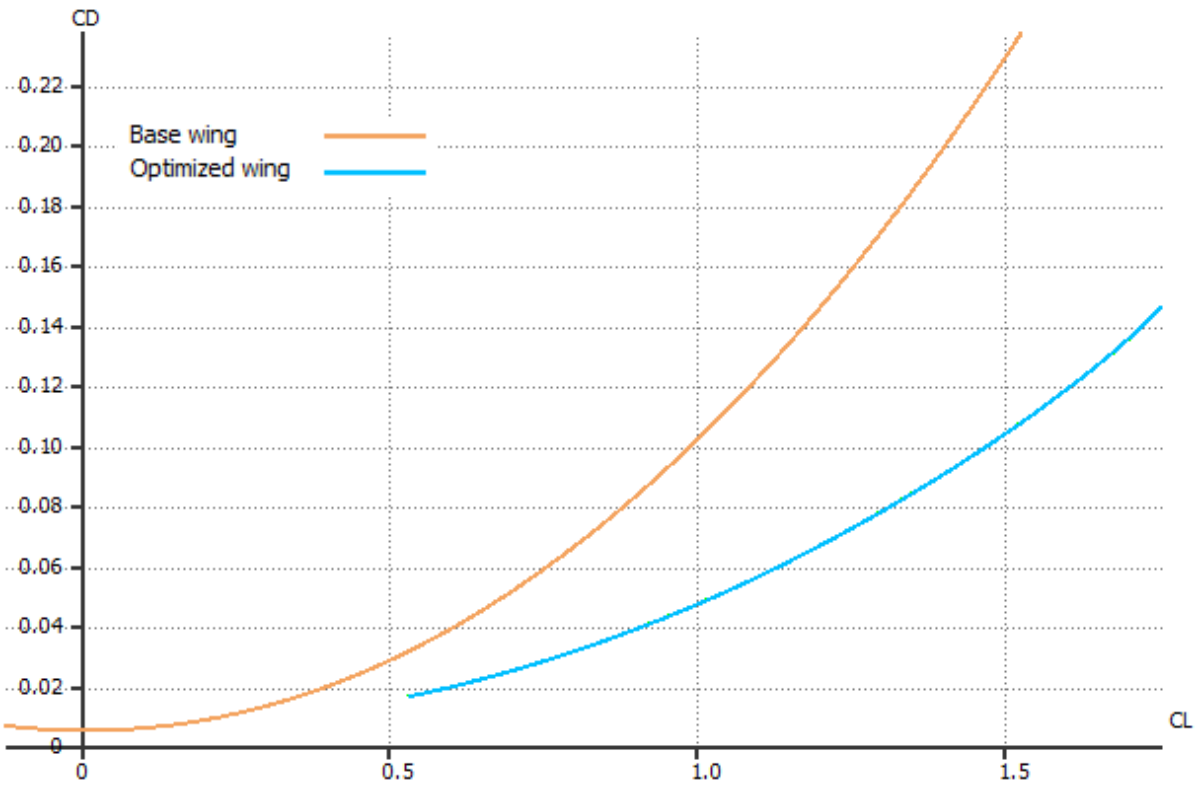
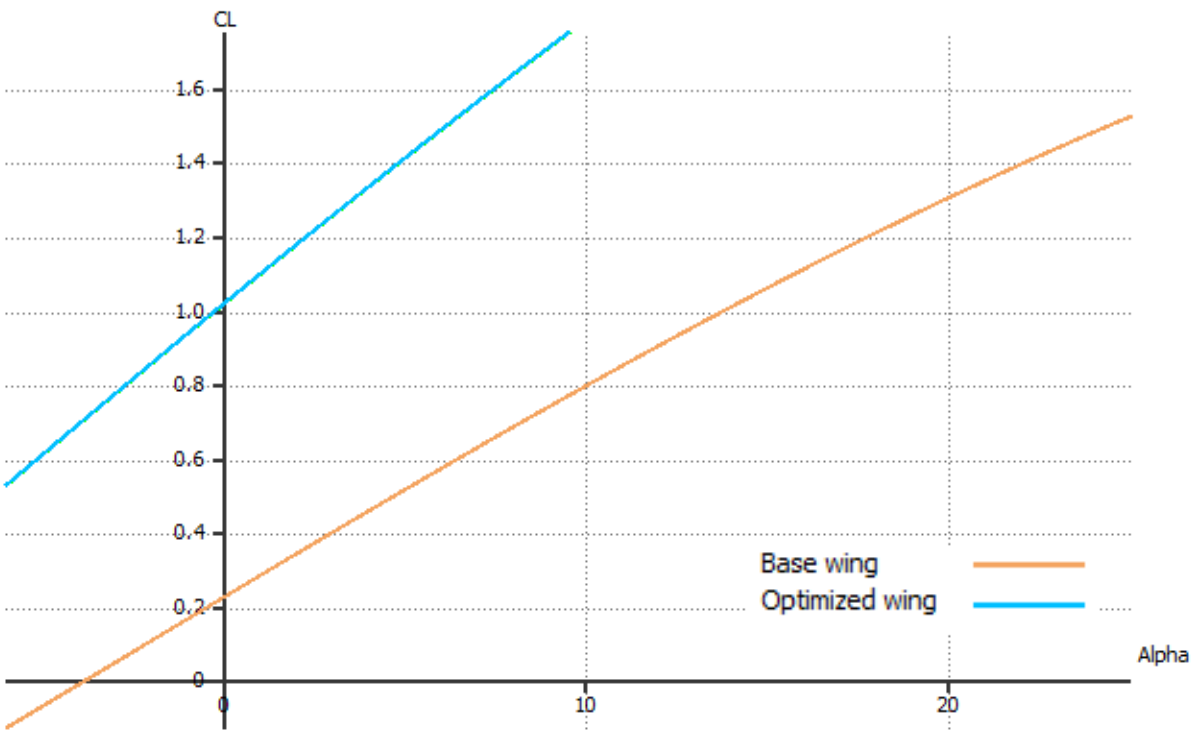*Figure 4. 2: Wing comparison, polar graph*

Figure 4. 3: Wing comparison, C_L vs α

One last graph that is of interest to analyze, in order to extract a quantitative measurement to evaluate the overall wing performance is the efficiency. In this case, the efficiency against the lift coefficient is reported (Figure 4.4). Similar to what occurred in the

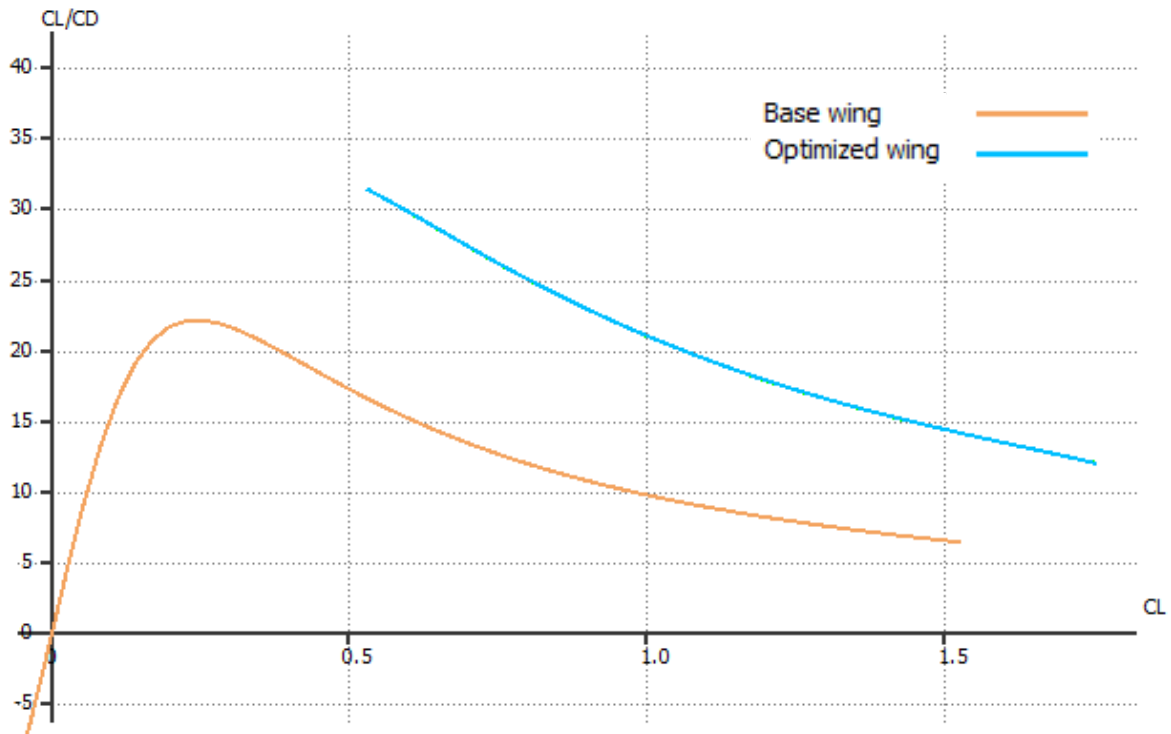previous graphs, the efficiency of the optimized wing, as expected, is higher at all lift coefficients.

Figure 4. 4: Wing comparison, Efficiency vs C_L

Of particular interest, the exact drag coefficient and therefore efficiency value should be examined at the design lift coefficient, previously established. These values can be seen in the following Table 4.

Wing	$C_D(C_{Ld})$	$E(C_{Ld})$
Base	0.063	12.2
Optimized	0.031	24.8

Table 4: Drag coefficient and efficiency of the optimized wing at the design lift

From the table it can be seen that the drag coefficient has been greatly reduced, halving in value. In fact, there is a significant efficiency difference of 12.6, which corresponds to an increase of 103% with respect to the base wing. In terms of range and endurance, these are improved too, as Breguet's equation for range is directly proportional to the aerodynamic efficiency, as seen below in equation (4). This means that if the efficiency is doubled, keeping the rest of the parameters unvaried, so will the range and endurance.

$$R = \frac{\eta}{SFC}\frac{C_L}{C_D}\ln\left(\frac{W_{initial}}{W_{final}}\right) \qquad (4)$$

5. Conclusion

Throughout this thesis the full preliminary design of a rescue UAV's wings has been carried out. The first chapter in this thesis introduced the urgent migration crisis occurring in the Mediterranean, explaining the current measures and the proposed solution. Using as a starting point the initial projection of Marangoni's aircraft, throughout the second chapter the mission and base geometry is defined. Several airfoils were analyzed and compared, selecting the NACA 4415 as the best option, which led to the beginning of the optimization process with the main objective of minimizing the drag to maximize the aerodynamic efficiency, developed in chapter 3. To reduce the overall drag, a taper ratio, higher aspect ratio and a wing twist was calculated and applied, this last being calculated using Prandtl's Lifting-Line theory using a Matlab script. These results were incorporated into the new wing configuration, carried out in chapter 4, which was then compared against the base wing in the XFLR5 software, observing a significant drag reduction. All numerical results are summarized in the table below.

Parameter	Optimized Wing
Airfoil	NACA 4415
Surface Area S	3.50 m^2
Wingspan b	5.20 m
Aspect Ratio AR	7.73
Taper ratio TR	0.31
Sweep angle λ	7.77º
Optimal Twist $\alpha(z) - \alpha_{L0}(z)$	Applied
Design lift coefficient C_{Ld}	0.77
Drag coefficient C_D at C_{Ld}	0.031
Efficiency C_L/C_D at C_{Ld}	24.8
Efficiency improvement	103%

Table 5: Summary of the final wing

6. Bibliography

[1] "Mediterranean: Missing Migrants Project." *Mediterranean | Missing Migrants Project*, https://missingmigrants.iom.int/region/mediterranean?region_incident=All&route=All& year%5B%5D=2500&month=All&incident_date%5Bmin%5D=&incident_date%5Bma x%5D=.

[2] Ansa. "The Main Migration Routes to the European Union." *InfoMigrants*, Infomigrants, 11 Nov. 2021,https://www.infomigrants.net/en/post/36391/the-main-migration-routes-to-the-european-union.

[3] Malakooti, Arezo, and Fall Chiara. "Migration Trends across the Mediterranean." *Global Initiative*, 11 Jan. 2021, https://globalinitiative.net/analysis/migration-dynamics-mediterranean/.

[4] Thevenin, Bruno. "Cambio En El Mar Mediterráneo." *El País*, 28 May 2021, https://elpais. Com/opinion/2021-05-28/cambio-en-el-mar.html.

[5] "El Helicóptero De Salvamento Helimer Necesita Como Mínimo 27 Minutos Para Ponerse a Punto Antes De Despegar." *Europapress.es*, Europa Press, 4 Jan. 2006, https://www.europapress.es/sociedad/noticia-helicopetero-salvamento-helimer-necesita-minimo-27-minutos-ponerse-punto-antes-despegar-20060104142407.html.

[6] "Salvamento Marítimo Mejora En 30 Minutos El Tiempo De Respuesta De Su Helicóptero En Baleares." *Murcia.com*, 27 July 2020, https://www.murcia.com/region/noticias/ 2020/07/27-salvamento-maritimo-mejora-en-30-minutos-el-tiempo-de-respuesta-de-su-helicoptero-en-baleares.asp#:~:text=A%20partir%20del%20d%C3%ADa%2027,del%20helic%C3% B3ptero%20ubicado%20en%20Palma&text=La%20respuesta%20ª%20una%20llama da,aguas%20de%20Baleares%20cada%20ª%C3%B1o.

[7] Insider Intelligence. "Drone Technology Uses and Applications for Commercial, Industrial and Military Drones in 2021 and the Future." *Business Insider*, Business Insider, 12 Jan. 2021, https://www.businessinsider.com/drone-technology-uses-applications ¿r=US&IR=T.

[8] Redacción. "Salvamento Marítimo Inicia Las Operaciones Con El Helicóptero No Tripulado Camcopter S-100." *Infodefensa*, Revista Defensa InfoDefensa, 12 July 2021, https://www.infodefensa.com/texto-diario/mostrar/3056152/salvamento-maritimo-inicia-operaciones-helicoptero-no-tripulado-camcopter-s-100.

[9] "CLS Has Signed a Contract with EMSA for Maritime Surveillance by Drones." *CLS*, 20 Oct. 2021, https://www.cls.fr/es/cls-tekever-have-signed-new-contract-for-maritime-surveillance-by-drones-with-euroepan-maritime-safety-agency/.

[10] Marangoni, Gioele. *Progettazione preliminare di un UAV ad ala fissa per il soccorso di natanti in panne*. Sapienza Università di Roma.

[11] "Basi Aeree." *Guardia Costiera*, https://www.guardiacostiera.gov.it/organizzazione/ Pages/basi-aeree.aspx.

[12] "Authority Map." *Hellenic Coast Guard*, https://www.hcg.gr/en/contact/map/.

[13] "87 Unidades Marítimas y Aéreas." *Salvamento Marítimo*, http://www.salvamentomaritimo.es/conocenos/nuestros-medios/87-unidades-maritimas-y-aereas.

[14] "EAM-T56." *EAM Worldwide*, https://eamworldwide.com/raft/eam-t56/.

[15] Selig, Michael. "UIUC Airfoil Data Site." *UIUC Applied Aerodynamics Group*, https://m-selig.ae.illinois.edu/ads/coord_database.html.

[16] "Drs Sentry HP. Specifications. A Photo." *Avia.pro*, 14 Nov. 2016, https://avia-pro.net/blog/drs-sentry-hp-tehnicheskie-harakteristiki-foto.

[17] "Aerojet SD-2 Overseer." *Military Wiki*, https://military-history.fandom.com/wiki/Aerojet_SD-2_Overseer.

[18] "Anka-S Unmanned Aerial Vehicle." *Airforce Technology*, 11 Apr. 2018, https://www.airforce-technology.com/projects/anka-s-unmanned-aerial-vehicle/.

[19] "General Description." *XFLR5*, 14 Jan. 2021, http://www.xflr5.tech/xflr5.htm.

[20] Marino, Luca. "Lecture 5." Aircraft and Helicopter Aeridynamics. Rome, Sapienza Università Di Roma.

[21] Molland, Anthony, and Stephen Turnock. "Finite Span." *ScienceDirect*, 2007, https://www.sciencedirect.com/topics/engineering/finite-span.

[22] Pinzón, Santiago. "Introduction to Vortex LattIce Theory." *ResearchGate*, Embry-Riddle Aeronautical University, Oct. 2015,https://www.researchgate.net/publication/314277432_Introduccion_a_la_teoria_VLM_Vortex_Lattice_Theory.

[23] Henderson, William P, and Bruce J Holmes. "Induced Drag – Historical Perspective." *SAE MOBILUS*, SAE Technical Paper Series, 1 Sept. 1989, https://saemobilus.sae.org/content/892341/.

[24] Phillips, W. F. "Lifting-Line Analysis for Twisted Wings and Washout-Optimized Wings." *Utah State University, Logan, Utah*, 2004.

[25] Garrison, Peter. "The Perfect Airplane Wing." *Smithsonian Magazines*, Smithsonian Institution, Feb. 2019,https://www.smithsonianmag.com/air-space-magazine/ perfect-airplane-wing-180971225/.

[26] Mangiantini, Carlo. *Design parametrico di un'ala di un UAV e stima delle prestazioni attraverso prove di volo con un prototipo in scala*. Sapienza Università di Roma.